

Department of Physics and Astronomy
University of Heidelberg

Master Thesis

in Physics

submitted by

Ole Schmidt

born in Rendsburg, Germany

2016

**Simulation and commissioning
of the rejection of late conversions
in the TRD triggers of ALICE**

**This Master Thesis has been carried out by Ole Schmidt at the
PHYSIKALISCHES INSTITUT
UNIVERSITY OF HEIDELBERG
under the supervision of
Prof. Dr. Johanna Stachel**

Abstract

The Transition Radiation Detector (TRD) of ALICE at the LHC provides level-1 trigger contributions based on the information of individual tracks, e.g. triggers on electrons and jets. Chamber-wise track segments are merged stack-wise in the Global Tracking Unit and used for the on-line reconstruction of transverse momentum (p_T) and electron identification. The dominant background of the single electron triggers originates from photon conversions into electrons and positrons at large radii, mostly in the material in front of the TRD. For these late conversions the p_T reconstruction via a straight line fit to the track segments overestimates the true p_T significantly.

In this thesis the on-line reconstruction of the track parameters is extended. The local curvature of the tracks is exploited to reject electrons and positrons from late conversions by evaluating their sagitta within the TRD layers. After successful tests in simulations, detailed instructions for the implementation of the tracking algorithm into the FPGA array were developed. Based on these instructions, the algorithm was implemented in hardware, preserving the 7 μ s latency of the trigger decision relative to a level-0 trigger.

The hardware design was verified through a commissioning process and the results agree on the bit-level with the software simulation. The performance of the late conversion rejection is presented, as well as prospects for TRD triggers for data taking in LHC Run 2. The rejections of the single electron triggers were maintained, and the efficiencies simultaneously increased. Furthermore, the late conversion rejection allows for a lower p_T threshold of the jet trigger, which might shift the bias on the fragmentation functions of the triggered jets to lower jet p_T .

Kurzfassung

Der Übergangsstrahlungsdetektor (TRD) des ALICE-Experiments am LHC trägt unter anderem mit Elektronen- und Jet-Triggern zur globalen Level-1 Triggerentscheidung bei. Die TRD Triggerentscheidungen beruhen auf Informationen von einzelnen Teilchenspuren, die in der globalen Spurrekonstruktionseinheit (GTU) aus Spursegmenten innerhalb einzelner Detektorstapel zusammengefügt werden. Die Spursegmente werden benutzt, um online sowohl den Transversalimpuls zu bestimmen, als auch Elektronen zu identifizieren. Elektronen und Positronen aus Paarbildungsprozessen von Photonen bei großen Radien, hauptsächlich im Material unmittelbar vor dem TRD, stellen den dominanten Untergrund der Elektronen-Trigger dar. Der in der GTU online durch die Annäherung einer Geraden an die Spursegmente berechnete Transversalimpuls (p_T) dieser sogenannten *Late Conversions* wird signifikant überschätzt.

In dieser Arbeit wird die lokale Krümmung der Teilchenspuren ausgenutzt und ihre Sagitta innerhalb des TRD berechnet, um online zwischen Late Conversions und primären Teilchen unterscheiden zu können. Nach erfolgreichen Tests in Simulationen wurde eine detaillierte Anleitung für die Implementierung des Algorithmus in der Hardware erstellt. Die Latenz von $7\ \mu\text{s}$ relativ zur Level-0 Triggerentscheidung bleibt von der Hardware-Implementierung unberührt.

Die Funktionsweise der Hardware-Implementierung wurde bestätigt. Die Ergebnisse der Berechnungen stimmen bitgenau mit denen der Simulation in Software überein. Neben der Leistungsfähigkeit des Algorithmus werden Perspektiven für die Trigger des TRD präsentiert. Die Anzahl an Ereignissen, die von den Elektronen-Triggern des TRD verworfen werden, bleibt konstant, während die Effizienz erhöht wird. Zusätzlich ermöglicht der Algorithmus eine niedrigere Schwellwertbedingung des Transversalimpulses für den Jet-Trigger. Hierdurch könnte eine durch den Trigger unverzerrte Auswahl von Jets bis hin zu niedrigeren p_T ermöglicht werden.

Contents

1. Introduction	1
1.1. Physics background	1
1.2. Large Hadron Collider	3
1.3. A Large Ion Collider Experiment	4
1.3.1. Detectors	5
1.3.2. Trigger system	7
1.4. Outline	8
2. Transition Radiation Detector	11
2.1. Principle of operation	11
2.2. Structure	14
2.3. Front-end electronics	14
2.4. Global Tracking Unit	16
2.5. On-line tracking algorithm	16
2.5.1. Tracklets	17
2.5.2. Combining tracklets to tracks	18
2.5.3. Transverse momentum reconstruction	19
2.6. TRD trigger contributions	20
3. Late conversions	23
3.1. Fake high- p_T tracks	23
3.2. Reconstruction of track parameters from sagitta	25
3.3. Identification of late conversions	27
3.4. Sagitta calculation	28
3.4.1. Simplification	32
3.4.2. Implementation in AliRoot GTU simulation	33
3.4.3. Possible optimizations	34
3.5. Proposal for hardware implementation	36
4. Commissioning	41
4.1. Hardware simulation with ModelSim	41
4.1.1. Tracklet files	42
4.1.2. Tracking output	42
4.1.3. Results	43
4.2. GTU test setup in Heidelberg	43
4.3. Results in Pb–Pb data taking	44

5. Performance and applications	47
5.1. Rejection of late conversions	47
5.2. Prospects for electron triggers	50
5.2.1. Event and track selection	51
5.2.2. PID and Δp_T^{-1} cut efficiencies	52
5.2.3. Results	53
5.3. Jet trigger	57
6. Summary and Outlook	61
A. GTU simulation	63
A.1. Output of the late conversion rejection	63
A.2. Performance for different optimization methods	63
A.3. Load custom tracklet files	65

1. Introduction

Probing the structure of elementary matter and its interactions at the most fundamental level is the main goal of experimental particle physics. The current understanding of these characteristics is embodied in the Standard Model, in which the interactions between particles themselves are described by the exchange of particles.

The Standard Model has proven itself extremely successful in describing current experimental data. However, it is not considered complete and fundamental. The model embraces many parameters, which need to be determined by experimental measurements. Furthermore, several eminent questions remain to be answered: The origin of the family structure as well as CP violation do not evolve from the theory. Gravitational force and dark matter are further examples which cannot be described by the Standard Model. These open questions are addressed in various particle physics experiments. For example, large particle accelerators produce controlled particle collisions with center of mass energies up to several TeV, which are observed by complex detectors.

Simply colliding two nuclear particles at these high energies is not feasible. Instead, the particle colliders accelerates particles in bunches consisting of some hundreds of billions of particles and after the particles have reached the desired energy, opposing bunches are bend to collide inside the detectors. In general, not all of the detectors can be read out continuously. In addition, the available disk space to store the produced data is not infinite. Hence, to initiate the readout of the detectors only at specific times, e.g., in case of bunch crossings inside the detectors, the experiments typically comprise different trigger systems. Amongst other detectors, the Transition Radiation Detector (TRD) of A Large Ion Collider Experiment (ALICE) at the Large Hadron Collider (LHC) at CERN contributes triggers on specific physics events to the ALICE trigger system. The subject of this thesis is the optimization of the trigger contributions of the TRD.

1.1. Physics background

The elementary particles included in the Standard Model (see Figure 1.1) can be sorted in three different groups, based on their spin: The particles with a spin of $\frac{1}{2}$ (fermions) are the basic constituents of matter. The mediating particles of the fundamental interactions (excluding the gravitational force) have a spin of 1 and are called gauge bosons. The Higgs boson with a spin of 0 gives the particles their mass.

The fermions are subdivided into quarks and leptons. Quarks partake in all fundamental interactions, namely the strong interaction mediated by the gluons, the weak interaction mediated by the W^\pm and the Z bosons and the electromagnetic interaction mediated by the photons. The leptons on the other hand partake only in the weak and

1. Introduction

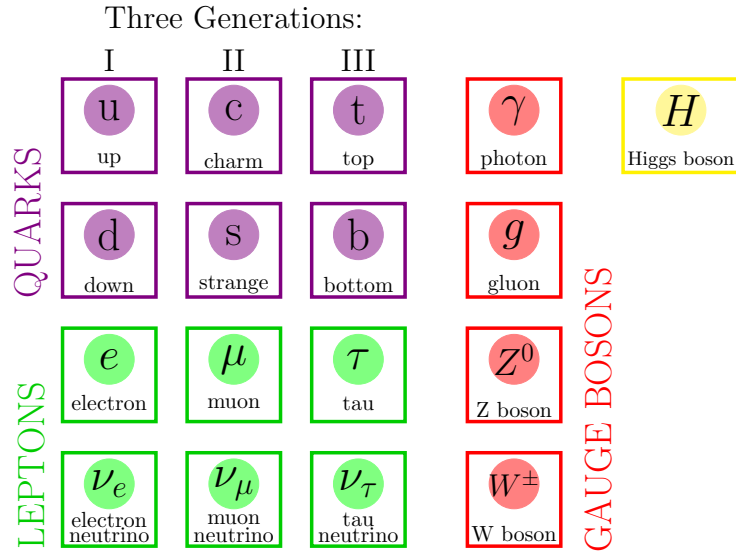


Figure 1.1.: The Standard Model of Particle Physics. The fermions (quarks and leptons) are organized in three generations. The forces are mediated by the gauge bosons. The Higgs boson generates the fermion masses [1].

electromagnetic interactions. All fermions also exist with opposite charges. These are called anti-particles.

The strong interaction couples to color charged objects, namely the quarks and the gluons. Free color charged objects have not been observed in experiments until now [2, 3]. This so-called confinement can be explained pictorially: When quarks are separated from each other, the potential in between the quarks increases linearly with their distance. The reason behind this is the color charge of the gluons themselves. If the distance between two quarks, and thus the energy, becomes large enough, new quark and anti-quark pairs are created. Hence, only color neutral objects can exist freely. However, the detailed mechanism of confinement is not yet fully understood and subject of ongoing research.

A state of liberated quarks and gluons is predicted at temperatures which existed shortly after the big bang [4, 5]. This so-called Quark-Gluon Plasma (QGP) can be created in nuclear reactions at beam energies such as delivered by the LHC: By colliding heavy nuclei at high energies, the temperature of the created matter is sufficiently high for the formation of a QGP.

A direct observation of the QGP is not feasible. Instead, appropriate probes shall reveal its properties. These probes include global event observables, e.g. the elliptic flow, a non-uniform variation in azimuthal direction of energy and momentum of the particles produced in the collisions [6, 7]. Additionally, strange quarks should exist in comparable numbers to those of up and down quarks and thus should give rise to an enhanced production of strangeness carrying particles [8]. Further examples for probes of the QGP include heavy-quark vector-resonances, such as the J/ψ , composed of a charm

and an anti-charm quark. To measure J/ψ in the di-electron channel $J/\psi \rightarrow e^+e^-$ the resulting electrons¹ must be well identified. Here, the Particle IDentification (PID) capabilities can give a decisive contribution. Particle jets depict another interesting probe for the QGP. Jets should show different characteristics, depending on whether they traverse the medium or not. Heavy-flavor quarks, studied via their semileptonic decays, allow to investigate the predicted mass hierarchy in energy loss mechanisms. In order to obtain statistical significance of these probes, a trigger on events of interest is required. A comparison between the measured probes in heavy-ion collisions and proton–proton collisions, as well as proton–ion collisions, is needed to draw conclusions about the characteristics of the QGP. Thus, triggers on the events of interest are needed in all of these collision systems. The on-line tracking capabilities of the TRD allow to select events likely containing quarkonia, open heavy-flavor and jets. This thesis mainly deals with purifying all of these event samples.

1.2. Large Hadron Collider

The need for ever greater energies in controlled particle collisions has lead to the conceptual design [9] and construction of the Large Hadron Collider (LHC) at CERN, the world’s largest particle accelerator today [10].

The LHC re-utilizes the tunnel originally built for the Large Electron-Positron Collider (LEP) about 100 m below the surface with a circumference of 26.7 km crossing the border between Switzerland and France near Geneva. To overcome the synchrotron radiation losses for the light electrons and positrons in LEP, the LHC collides protons at a design beam energy of 7 TeV and lead nuclei at an energy of 2.76 TeV per nucleon. The highest beam energy translates to a dipole field of ~ 8.33 T for the deflecting magnets to keep the particles on track. To achieve this, the dipole magnets have to be superconducting. A twin-bore magnet was chosen, which is cooled via liquid helium to below 2 K. Besides the high beam energies, also very high beam intensities are needed to collect a sufficient amount of statistics for rare processes. This ruled out the use of protons and opposing anti-protons, which can be bend by the same magnetic field.

Before the particles are injected into the LHC with an energy of 450 GeV (protons) or 177 GeV per nucleon (nuclei), they have to pass a pre-acceleration chain. Protons and ions pass different linear accelerators before they are injected into the BOOSTER (protons) or LEIR (ions), respectively. Both are then injected into the Proton Synchrotron and finally the Super Proton Synchrotron as last stage of the pre-acceleration chain. Figure 1.2 gives an overview of the LHC. Intersecting the tunnel, the major experiments installed around Interaction Points (IP) at four of the eight straight sections are shown.

- **ATLAS** (A Toroidal LHC Apparatus for Spectroscopy) and **CMS** (Compact Muon Solenoid) are multi-purpose detectors with similar physics objectives installed at IP 1 and IP 5, respectively. ATLAS is the largest volume detector with a length of 46 m, a diameter of 25 m and a weight of 7000 t. The CMS experiment comprises a

¹In the following, electrons refer to both e^- and e^+ .

1. Introduction

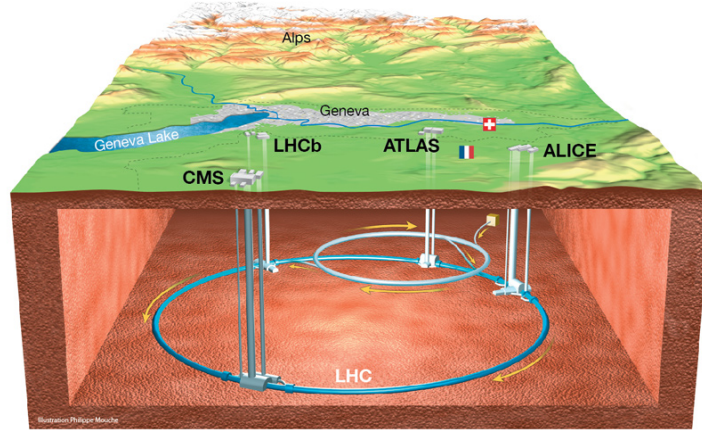


Figure 1.2.: Overall view of the LHC including the main experiments ATLAS, CMS, LHCb and ALICE. The experiments are located in underground caverns that are connected to the surface by 50 m to 150 m long vertical tunnels. Part of the pre-acceleration system is drawn in light blue. Image: CERN [13].

superconducting solenoid offering a magnetic field of 4 T enabling the measurement of high energetic muons. In 2012, ATLAS and CMS discovered the Higgs boson [11, 12].

- **LHCb** (Large Hadron Collider beauty) is specialized in beauty-physics, measuring the parameters of CP violation in the interactions of b-hadrons. Such studies can help to explain the asymmetry between matter and antimatter in the universe. Since pairs of b-quarks are predominantly produced in the same forward (or backward) cone, LHCb is a single arm forward spectrometer.
- **ALICE** (A Large Ion Collider Experiment) is the dedicated heavy-ion experiment with its focus on studying the properties of the Quark–Gluon Plasma (QGP). ALICE is described in more detail in the following Section 1.3.

1.3. A Large Ion Collider Experiment

A Large Ion Collider Experiment (ALICE) [14, 15] is the only experiment at the LHC specifically designed to study strongly interacting matter at extreme energy densities as created in central heavy-ion collisions. It aims to investigate the properties of the Quark–Gluon Plasma (QGP) assumed to be formed in such collisions as delivered by the high beam energies of the LHC. Measurements of proton–proton collisions as well as of proton–nuclei collisions serve as a reference and are used to determine non-QGP nuclear effects, i.e. differences between free protons and protons bound together with neutrons in a nucleus. Due to the high multiplicity environment of heavy-ion collisions, this task requires a robust, highly comprehensive and versatile detector.

ALICE has been designed for track reconstruction with rapidity densities of charged particles up to $dN_{ch}/dy \sim 8000$, which was the highest conceivable estimate at the time the experiment was designed². Good tracking resolution for high- p_T probes, such as jets or electrons from heavy-flavor decays, is needed as well as tracking down to very low transverse momenta for the measurement of total particle yields. The latter are an important parameter for the global event characterization and must be determinable by ALICE. Further parameters which have to be determined are centrality and event plane. For this purpose, scintillator arrays are installed at large pseudo-rapidities. For the determination of the chemical composition of the produced particles, Particle IDentification (PID) is also extremely important. Multiple detectors exploiting various physics processes provide the necessary PID capabilities. Overall, the experiment is designed as a multi-purpose detector for physics at mid-rapidity and the forward region.

The experiment has inherited the large octagonal magnet from the L3 experiment at LEP, which provides a modest solenoidal drift field of 0.5 T along the beam direction for the onion-like structured detectors inside the magnet. The muon spectrometer in forward direction is installed behind an absorber. It consists of a warm dipole magnet with integrated horizontal field of 3 Tm, six tracking stations and additional trigger stations behind further iron shielding.

1.3.1. Detectors

The experimental setup of ALICE is shown in Figure 1.3. Only detectors relevant for this thesis will be described. This includes the major tracking detectors of the central barrel as well as detectors contributing triggers relevant for the triggers of the Transition Radiation Detector (TRD). In the global coordinate system of ALICE, the z -axis lies parallel to the beam direction. The transverse plane is spanned by the x - and y -axis.

In immediate vicinity to the beam pipe, the Inner Tracking System (ITS) [16] is installed. It consists of six barrels of high-resolution silicon-based detectors for primary and secondary vertex reconstruction and tracking of low-momentum particles. Two layers respectively of Silicon Pixel (SPD), Silicon Drift (SDD) and Silicon Strip Detectors (SSD) are used for efficient pattern recognition and impact parameter resolution. The SPD provides triggers for centrality and minimum bias events.

Outside of the ITS, the main tracking system of ALICE, the cylindrical Time Projection Chamber (TPC) [17], is installed. It fully covers a pseudo-rapidity interval of $|\eta| \leq 0.9$ and has an inner and outer radius of 0.85 m and 2.47 m respectively. The central high-voltage electrode has a potential difference of 100 kV with respect to the end plates, which are equipped with Multi-Wire Proportional Chambers (MWPCs) with analog pad readout. This allows to measure the amount of charge deposited by primary ionization of the traversing particles and, hence, their specific energy loss, leading to particle identification (see Figure 1.4). From 2015 on, the gas mixture of the TPC is Ar-CO₂. Until 2011 it was operated with Ne-CO₂-N₂ and between 2012 and 2015 with

²The most central collisions of two lead nuclei at $\sqrt{s} = 2.76$ GeV in the Pb-Pb periods in 2011 and 2012 resulted in particle multiplicities of $dN_{ch}/dy \sim 1600$.

1. Introduction

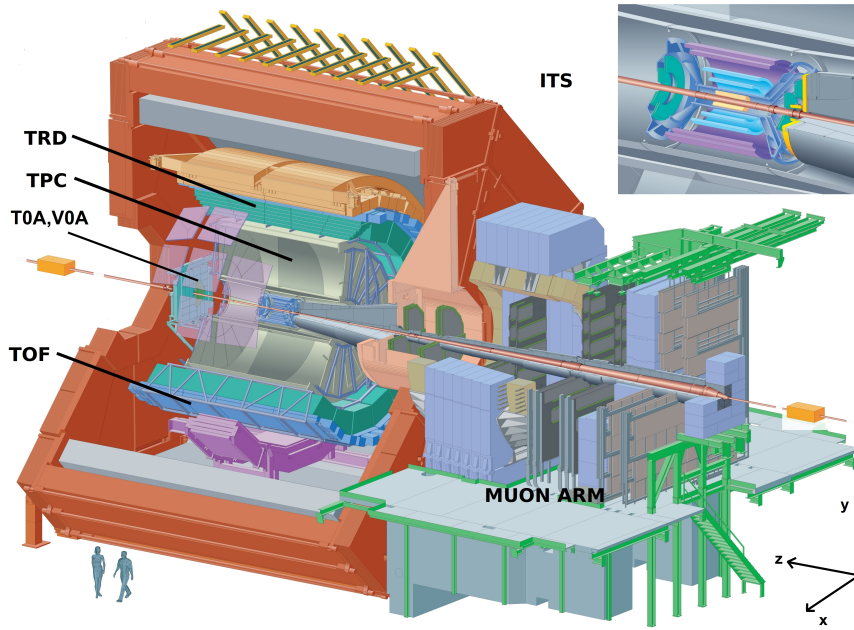


Figure 1.3.: ALICE detector setup. The central barrel is located inside the L3 magnet (red). The Transition Radiation Detector (TRD) surrounds the Time Projection Chamber (TPC) and the Inner Tracking System (ITS). Forward detectors (T0, V0) are installed on both sides of the interaction region. The Time-Of-Flight (TOF) detector surrounds the TRD.

Ne-CO₂. The resulting drift time is about 95 μ s, the momentum resolution is about 7 % at 10 GeV/c and the dE/dx resolution is about 5 % [18].

Next to the TPC, between a radius of 2.9 m and 3.7 m, the TRD [19] is installed. It is designed for electron identification also in the high-multiplicity environment of heavy-ion collisions. Furthermore, it contributes to the global tracking and provides various triggers for high transverse momentum processes as well as for leptonic decays. The aspects of the TRD relevant for this thesis will be discussed in detail in the dedicated Chapter 2.

The Time-Of-Flight (TOF) array [20] located at a radius of 3.7 m provides a timing resolution better than 100 ps at an occupancy below 10 % by the use of multi-gap resistive plate chambers. This allows to determine the mass of high-energy particles, as long as their velocity is significantly below the speed of light.

Part of the central barrel acceptance is equipped with electromagnetic calorimeters. The ElectroMagnetic CALorimeter (EMCAL) is composed of Pb scintillator sandwiches and has an overlap with the TRD. The PHOTon Spectrometer (PHOS) has no overlap with the TRD. Both calorimeters can be used for triggering.

Two wheels of scintillator panels and 12 quartz Cherenkov counters on either side of the interaction point, named V0 and T0, respectively, provide minimum bias triggers for the experiment.

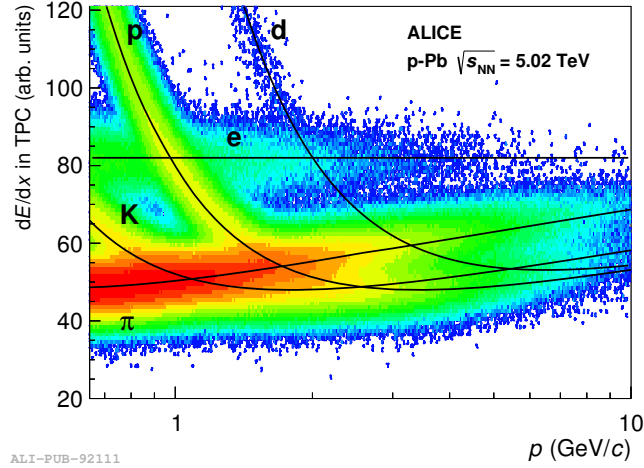


Figure 1.4.: This plot shows the specific energy loss dE/dx of detected particles in the TPC. The different bands of the particle species are labeled and the parametrizations are drawn as solid lines. For high momenta the electron and the pion bands start to overlap [21].

1.3.2. Trigger system

The maximum readout time of the major tracking device of ALICE, the TPC, varies from 300 Hz for Pb–Pb collisions to 1.4 kHz for p–p collisions [18]. Comparing these numbers to the typical interaction rates in the experiment during LHC Run 1 which were about 3–4 kHz for Pb–Pb and $O(100\text{ kHz})$ for p–p collisions [22], obviously not all events can be recorded. On the other hand, events that are of particular interest with respect to the physics objectives, are typically rare. E.g. a cross section for rare probes of the order of $\approx 100\text{ }\mu\text{b}$ corresponds to a probability per collision of $\approx 10^{-5}$ [19]. Therefore, it is necessary to implement an event filtering system, the so-called trigger system, that initiates the readout of all detectors only for the events of interest.

The maximum readout rates of the detectors depend on the collision system. For central heavy-ion collisions they vary between a few 10^4 Hz for the fastest detectors, e.g. V0, T0, SPD and TOF, to about 300 kHz for the large TPC with a drift time of about $100\text{ }\mu\text{s}$ as mentioned above. To allow for a significant reduction of the dead time of the whole experiment, the slower detectors should not need to be readout for events which could have been rejected already at an earlier stage by the faster detectors. Therefore, the trigger system of ALICE is subdivided into three different hardware levels based on timing plus one higher software level. A Central Trigger Processor (CTP) evaluates the different trigger signals and issues either an accept or a reject signal to the detectors.

The level-0 and level-1 trigger signals are generated within a fixed time with respect to the interaction to make selections on centrality and specific physics events. The fastest detectors at level-0 contribute mostly minimum bias triggers and triggers on multiplicity and sprays of particles in a narrow cones (jets), whereas the trigger contributions at level-1 add triggers on other selective physics signatures. The level-2 trigger about $100\text{ }\mu\text{s}$ after

1. Introduction

trigger level	timing	limited by	limit
level-0	$\sim 1.2 \mu\text{s}$ after int.	dead time	$\sim 100 \text{ kHz}$
level-1	$7.0 \mu\text{s}$ after level-0 for Run 2	readout bandwidth	$\sim 2.5 \text{ kHz}$
level-2	$\sim 100 \mu\text{s}$ after int.	input to High-Level Trigger	$\sim 1.5 \text{ kHz}$
HLT		1 GB/s to tape	

Table 1.1.: Overview of the different trigger levels of ALICE. The indicated limits are specific for the TRD in p–p operation.

the interaction allows for past-future protection of the TPC³ since Pb–Pb collisions with pile-up were considered non-reconstructible. A software trigger named High-Level Trigger (HLT) analyzes the complete data from TPC, TRD and other detectors, thus allowing for further event filtering, while already compressing it. An overview of the different trigger levels is given in Table 1.1.

The TRD contributes several physics triggers at level-1. A detailed listing of the TRD triggers used for Run 1 will be given in Section 2.6. This thesis comprises an expansion of the on-line tracking algorithm of the TRD to allow for additional background rejection of the triggers. A priori the timing requirements for the expansion are not known. The latency of the level-1 triggers was thus increased by 500 ns from $6.5 \mu\text{s}$ in LHC Run 1 to $7 \mu\text{s}$ in Run 2 to enable a more complex tracking algorithm.

It shall be emphasized that triggering on the higher levels implies an increase of the dead time for all detectors on lower trigger levels. Until the trigger decision on the higher level is made, a busy signal prevents the acceptance of a new lower level trigger. In addition, a high level-0 input rate is needed if triggering on rare events is planned.

1.4. Outline

This thesis is organized as follows: Chapter 2 begins with a description of the Transition Radiation Detector. The focus here lies on its trigger capabilities which are based on an on-line tracking algorithm. The transverse momentum of tracks is calculated from the offset of a straight line fit of the track to the nominal vertex. The selection of electrons originating from the primary vertex is contaminated by electrons originating from photon conversions in the supporting material in front of the TRD. These electrons, the so-called *late conversions*, pose the main background for the single electron triggers of the TRD.

Chapter 3 describes how the on-line track reconstruction can be extended by an approximation of the sagitta of the tracks. This feature allows for the identification and therefore the rejection of late conversions and is implemented in the software simulation of the on-line tracking algorithm. The commissioning process of the hardware implementation of the late conversion rejection is described in Chapter 4.

It is shown that the implementation in the hardware agrees with the software simulation. Thus, the expected trigger performance can be determined via re-running the

³The readout can be aborted in case different events overlap inseparably in the TPC.

simulation for recorded minimum bias events with the results presented in Chapter 5. The last Chapter 6 summarizes the results and gives an outlook on the Run 2 trigger prospects for the TRD⁴.

⁴From Run 3 on only minimum bias data taking is foreseen.

2. Transition Radiation Detector

The following Chapter gives an overview of the fundamental principles of particle tracking, electron identification and triggering with the Transition Radiation Detector (TRD) of ALICE. The focus lies on the global on-line tracking algorithm, which is extended to reject late conversions as described in Chapter 3.

In general, particles can be identified by their invariant mass, which in turn can be determined using different observables. One possibility is the time of flight measurement to a known distance as long as the time resolution allows to separate the different particle species. Considering velocity versus momentum, particle bands are formed for the different particle species dependent on their mass.

Another approach is to measure the specific energy loss dE/dx of charged particles traversing the active detector volume. It depends on $v/mc = \beta\gamma$ as described by the Bethe-Bloch formula [3], and thus for fixed momenta on the mass. This observable is measured by the Inner Tracking System (ITS), the Time Projection Chamber (TPC) and also the TRD.

However, at momenta in the relativistic rise of the Bethe-Bloch formula ($\beta\gamma \gtrsim 4$), the weak mass dependence complicates particle identification, especially the separation of the electrons from the much more abundant pions. A measurement of J/ψ in the di-electron channel requires the rejection of pions for off-line analyses by a factor of 100 while the electron efficiency must not fall below 90% [23].

The production of Transition Radiation (TR) by charged particles crossing the boundary surface between two media with different refractive indices predicted by Ginzburg and Frank in 1946 [24] and confirmed in the 1960s can be used to separate electrons and pions. TR becomes relevant only for Lorentz factors $\gamma \geq 1000$ [22] and the Lorentz factor is dependent on the particles mass ($\gamma = E/mc^2$). Hence, TR is caused exclusively by electrons at momenta relevant in the ALICE experiment. The probability to produce transition radiation at a single boundary crossing is very low ($\sim \alpha = 1/137$). Therefore, radiators are used which are typically composed of a stack of $O(100)$ thin foils or unstructured material where traversing particles cross many boundaries. The energy of the transition radiation photons in the ALICE TRD is in the X-ray range.

Exploiting this unique electron feature, the TRD was proposed and designed to add additional electron/pion separation from 1 GeV/c up to high momenta to the central barrel.

2.1. Principle of operation

A schematic cross-section of a TRD chamber can be seen in Figure 2.7. The basic entities of the detector are Multi-Wire Proportional Chambers (MWPCs), preceded by a drift

2. Transition Radiation Detector

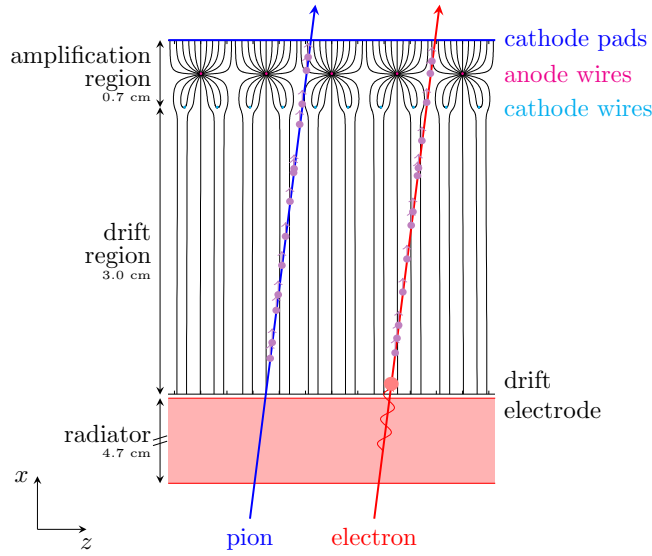


Figure 2.1.: A pion and an electron traverse a TRD chamber in the x - z -plane. The x -axis points away from the interaction point in radial direction, the z -axis lies in beam direction. Charged particles ionize the gas resulting in the production of electron clusters along the way which drift towards the amplification region in the electric field. In the sketched case the electron produces a TR photon in the radiator which is absorbed close to the entrance of the drift region due to the high photon absorption coefficient of the detector gas. The signals are read out at the cathode pads [25].

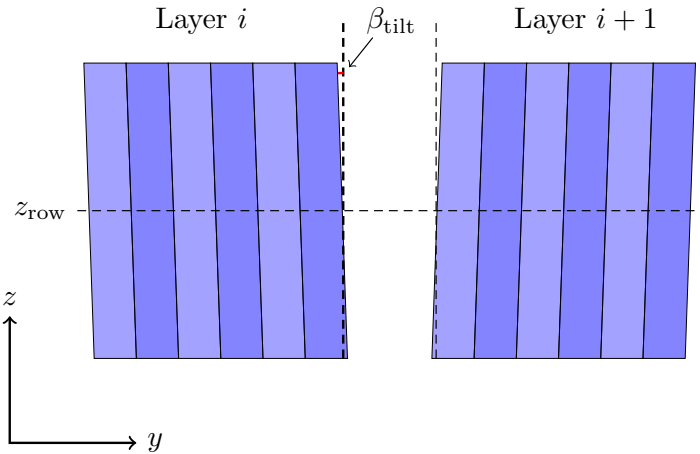


Figure 2.2.: Pads of neighboring layers are tilted in different orientation by β_{tilt} . This improves the z -position resolution for the off-line tracking. Adapted from [19].

region and a radiator. Charged particles deposit energy by ionizing the detector gas. In the amplification region thin wires are supplied with positive high voltage (anodes) leading to a strong electric field in close vicinity of the wires in which electrons gain energy and provoke avalanches by repeated collisions. On the cathode plane the movement of the created charges (mainly the ion drift) leads to a detectable signal. To obtain a good position resolution, the cathode plane is segmented into pads with an area of $A \approx 0.8 \text{ cm} \cdot 8 \text{ cm} = 6.4 \text{ cm}^2$. The granularity of the pads is high in the bending plane to match the tracking information of the TRD to that of the TPC. This way, the lever arm of the track reconstruction in ALICE is extended leading to an improved p_T resolution at high p_T .

The coarse granularity for the z position can be partially recovered during off-line tracking, since the pads of neighboring layers are tilted by a tilting angle $\beta_{\text{tilt}} = 2^\circ$ in opposite direction as shown in Figure 2.2. The pad tilting leads to a correlation of the position measurement in y and z , which depends on β_{tilt} .

To obtain a directional segment of a track rather than a single space point, the amplification region is preceded by a drift region with a length of 3 cm. The nominal drift field of $\sim 700 \text{ V cm}^{-1}$ leads to an electron drift velocity of $1.56 \text{ cm } \mu\text{s}^{-1}$. Hence, electrons from ionization produced at the beginning of the drift region have a drift time of about $2 \mu\text{s}$. The measurable deflection allows for correct track matching and a charge deposition measurement while the latency requirements for the trigger contribution are maintained because of the short drift time. Xenon is chosen as a counting gas due to its high absorption coefficient for X-ray photons. 15% of CO_2 is added as a quencher.

The TR photons are produced in the radiator in front of the chamber. A 48 mm sandwich setup of Rohacell HF71 foam and polypropylene fibers was chosen as a compromise between TR efficiency and mechanical properties such as stability. It results in the production of ~ 1.45 TR photons on average for a traversing charged particle with $\gamma \geq 1000$ [26].

The average pulse height for many tracks of electrons and pions within one chamber is shown in Figure 2.3. Gas ionization on both sides of the amplification wires leads to the characteristic peaks at the beginning of the signal. After this peak, the signal is induced only by the charges moving in the drift region. Since the electrons overall deposit more charge within the chamber compared to pions at a given momentum, the total charge deposition can be translated into an electron probability.

If a TR photon is absorbed, not only the total amount of deposited charge increases, but the signal also shows a characteristic peak at the end of the drift. TR photons produce electrons close to the entrance of the traversing particle into the chamber due to the high absorption coefficient for X-ray photons of the detector gas.

Thus, if the charge deposition is sampled in two different time bins, the charge deposition in the second time bin will be higher than in the first time bin for electrons.

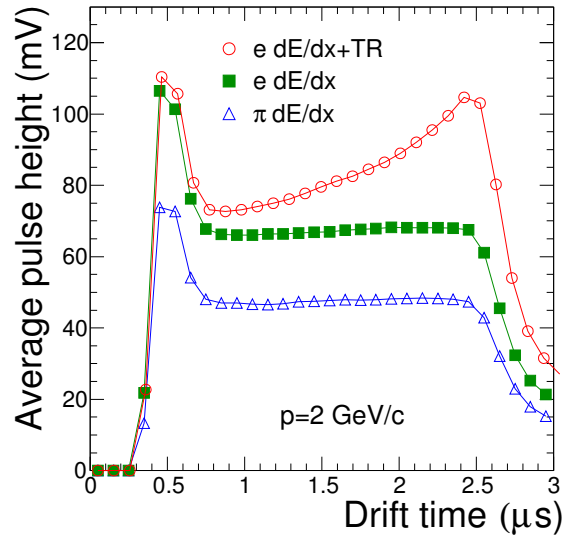


Figure 2.3.: Average pulse height for electrons and pions. In case of emitted TR photons, a peak rises at the end of the pulse. The peak at the beginning of the pulses originates from gas ionization on both sides of the anode wires [19].

2.2. Structure

The TRD covers the full acceptance of the central barrel, i.e., a pseudo-rapidity interval of $-0.9 \leq \eta \leq 0.9$ and the full azimuthal angle φ . It is segmented into eighteen sectors called supermodules in φ to match the segmentation of the TPC in the space frame of ALICE. The layered structure is driven by the need of good pion rejection. A short drift region enables fast on-line tracking. Six layers in radial direction r were found to be the optimal choice regarding pion rejection and cost [25]. Furthermore, to arrive at manageable chamber sizes, each supermodule comprises five stacks in longitudinal direction. An overview of the full TRD is given in Figure 2.4.

2.3. Front-end electronics

To fulfill the low latency requirements of the level-1 trigger decision, the recorded data must be processed as early as possible and as parallel as possible. The first step of the data processing is done by the Multi-Chip Modules (MCM, see Figure 2.5), which are mounted directly on top of the readout chambers and are connected to 18 pads within one pad row each. The edge channels are shared between adjacent MCMs to avoid inefficiencies at the boundaries. The MCMs comprise two custom chips, a Pre-Amplifier and Shaper Amplifier (PASA) and a TRAcklet Processor (TRAP), respectively.

First, the registered pad charges have to be amplified on the PASA, as the generated signal is very small¹, and converted to a voltage on a pedestal value. Additionally, the

¹For a minimum ionising particle the generated signal corresponds to about 10^5 electrons [27].

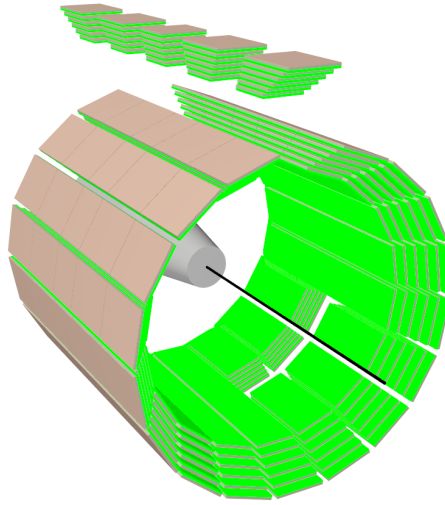


Figure 2.4.: Overview of the full TRD: It consists of 6 layers of tracking chambers in radial direction and is segmented in 18 sectors in azimuth and 5 stacks in longitudinal direction. The middle stacks of three supermodules (bottom right of the figure) are not installed in order to reduce the material budget in front of the PHOS calorimeter. [26]

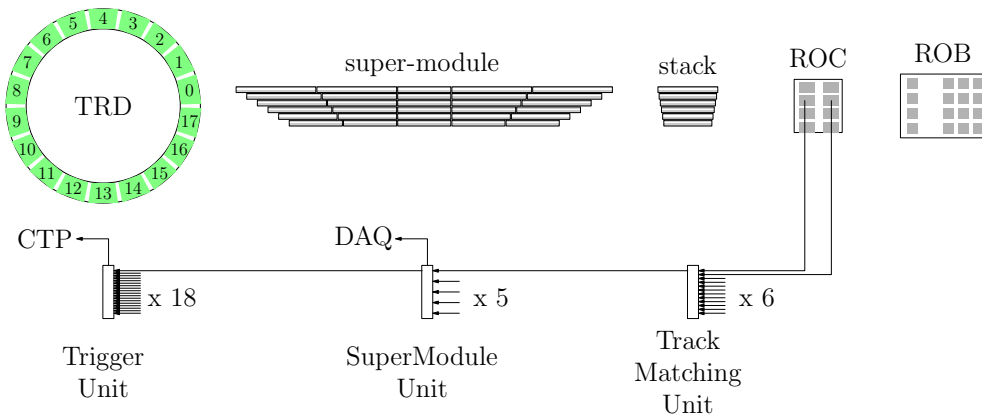


Figure 2.5.: Overview of the TRD readout: The top row shows the detector structure from the full installation of the eighteen sectors on the left to the individual ReadOut Boards (ROB) with 16 MCMs on the right. The ReadOut Chamber (ROC) sends its data via two optical links at 2.5 Gbit/s to the Track Matching Unit (TMU) which performs stack-wise tracking and has a buffer for the raw data of four events. The SuperModule Unit (SMU) hosts the trigger logic and the uplink to the Data Acquisition (DAQ). The interface to the Central Trigger Processor (CTP) is built by a TriGger Unit (TGU). All TMUs, SMUs and the TGU together build the Global Tracking Unit (GTU) of the TRD [26].

2. Transition Radiation Detector

PASA shapes the signal.

Second, the signal is converted to digital values by the Analog to Digital Converters (ADC) of the TRAP. The ADC sampling rate of 10 MHz translates into measuring ~ 20 points for a drift time of $2\ \mu\text{s}$ and a radial position resolution of about $150\ \mu\text{m}$.

After several filter stages and preprocessing, the digitized data are stored in an event buffer to be read out in case an accept signal for the level-1 trigger is issued by the CTP (L1a). After the drift time the data are shipped to the four CPUs of the TRAP where the hits for the charge clusters of two neighboring pads are approximated by a straight line to form on-line track segments. These track segments are referred to as *tracklets* and will be discussed in more detail in Section 2.5.1.

The data are merged in several stages from the individual MCMs on the ReadOut Boards (ROBs) for one half-chamber and sent via optical fibres to the Global Tracking Unit (GTU) situated outside of the L3 magnet. The same readout interface as for the tracklets is used for the raw data.

2.4. Global Tracking Unit

The GTU performs the global on-line tracking and hosts the uplink to DAQ as well as the interface to the CTP. It consists of one Track Matching Unit (TMU) per detector stack which receives the input of the corresponding 12 half-chambers (see Figure 2.5). Each TMU hosts an FPGA where the arriving tracklets are used as a basis for a fast tracking algorithm to form tracks through the detector. These tracks are used for the level-1 trigger decision of the TRD.

Next to performing the tracking algorithm, the TMU buffers the raw data for later transmission to the Data AcQuisition (DAQ) system in case of an level-2 accept signal (L2a) from the CTP. All tracks of one supermodule are merged in a SuperModule Unit (SMU) which generates the trigger decision and sends it via the Trigger Unit (TGU) to the CTP. The SMU also hosts the uplink to the DAQ system.

2.5. On-line tracking algorithm

In this section, the on-line tracking algorithm of the TRD is introduced [28]. As it is bound by the tight timing constraints of a level-1 trigger decision, it is massively parallelized and starts already at the individual MCMs of the readout chambers. Here, charge clusters are converted into tracklets. This part is referred to as local on-line tracking and will be shortly described in Section 2.5.1. For a more detailed description see [26, 28].

The basis of this thesis is the global on-line tracking performed by the TMUs of the GTU which is described in Section 2.5.2. Tracklets from the six readout chambers of a stack are matched to form longer tracks and their transverse momentum as well as their PID is calculated. This information is the basis for flexible and versatile trigger contributions by the TRD at level-1.

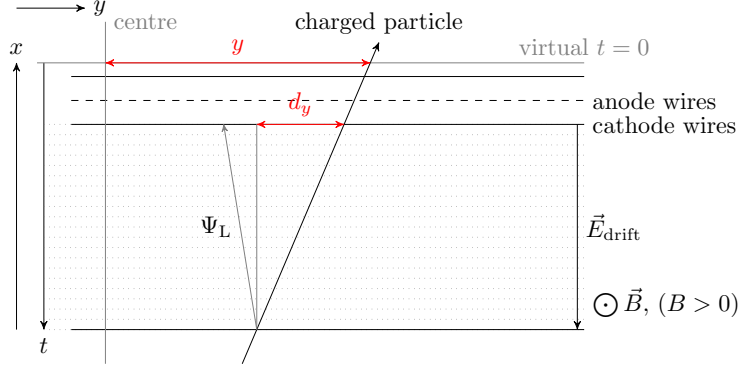


Figure 2.6.: A charged particle traverses a readout chamber of the TRD. Clusters detected at the beginning of the drift time (virtual $t = 0$) determine the y -position with respect to the center of the chamber. The deflection d_y is calculated from the clusters over the drift time and needs to be corrected for the Lorentz angle Ψ_L . The z -position is known from the padrow and PID information is obtained via the sum of the deposited charge of the clusters [26].

For the description of the tracking algorithm, a local coordinate system is used for each supermodule: The x -axis of the global coordinate system (see Figure 1.3) is rotated around the azimuthal angle to point to the center of the readout chambers. The z -axis remains in beam direction and the y -axis thus lies in the bending plane.

2.5.1. Tracklets

A particle traversing a TRD chamber can be detected by its energy deposition in the active volume of the detector as described in Section 2.1. In the MCMs, the digitized and filtered signal is used for the calculation of the tracklets.

The idea of the calculation is shown in Figure 2.6. The y -position of a cluster with respect to the center of the chamber is calculated as the center of gravity of the induced signal on three adjacent pads. Additive corrections have to be applied to compensate for distortions due to the simplified position calculation [29].

In order to obtain the deflection d_y of the tracklet, a simple straight line is assumed for the trajectory in the transverse plane, which is a good approximation for primary tracks. As the electrons from ionization move in an electrical drift field perpendicular to the magnetic field they are affected by a Lorentz drift. Additionally, the pad tilting leads to a slight deterioration of the resolution in y . Both are corrected using additive constants calculated in advance for each MCM [28].

A cut on the transverse momentum is done already on tracklet level to reduce the number of tracklets shipped to the GTU: $p_{T,\min}^{\text{local}}$ is translated to a minimum and a maximum deflection, respectively. At the moment $p_{T,\min}^{\text{local}} = 2.3 \text{ GeV}/c$ is used as threshold. The deflection is compared to the deflection of a track with infinite p_T . Tracklets with a deflection out of this range are rejected.

The z -coordinate is determined by the padrow, which varies between 0 and 15. The

2. Transition Radiation Detector

parameter	granularity	physical range	bits
y	$\frac{1}{160 \mu\text{m}}$	-64.32 cm to 64.32 cm	13
d_y	$\frac{1}{140 \mu\text{m}}$	-8.8 mm to 8.8 mm	7
z	1	0 to 15	4
PID	1	0 to 255	8

Table 2.1.: Overview of the content of the individual tracklet words.

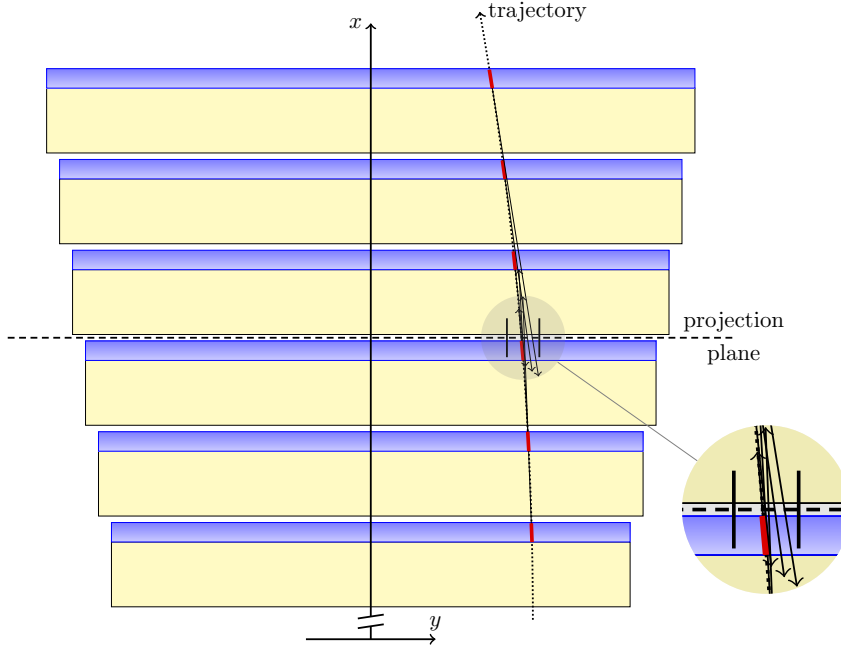


Figure 2.7.: Track matching in the x-y plane. The found tracklets (red) are elongated to the projection plane in the middle of the stack. Adapted from [28].

on-line PID is based on the deposited charge of a tracklet. The total amount is used to obtain the electron probability from a look-up table [30]. The probability between zero and one is translated into integer values from 0 to 255.

The tracklets are shipped to the GTU encoded in a 32-bit word. This word contains the y -position with respect to the center of the chamber (13 bits, signed), the deflection d_y (7 bits, signed), the z -row (4 bits, unsigned) and the PID value (8 bits, unsigned). Table 2.1 summarizes the tracklet word content.

2.5.2. Combining tracklets to tracks

The tracklets from the 12 half-chambers of one detector stack are sent to the corresponding TMU where they are matched to form tracks. The idea of the track matching is as follows:

1. Tracklets originating from the same track will have a similar angle α with respect to the primary vertex. Thus, their y -positions lie on a straight line in the x - y plane with a similar slope $\frac{\Delta y}{\Delta x}$.
2. Since only primary tracks shall be taken into account, the z -position of the tracklets lies on a straight line in the x - z plane with the interaction point (see bottom plot in Figure 2.9).

To test these conditions for all tracklets of the stack, they are projected onto a virtual y - z plane in the middle of the detector stack. If the projected coordinates for at least four tracklets from different layers fall into a window of configurable size and their angles α are consistent, they will be matched to form a track.

This matching cannot be done iteratively for all possible combinations of tracklets, as the available computing time is very limited. Furthermore, no handshaking exists between MCMs and TMUs to avoid additional deadtime. Hence, a more sophisticated algorithm is implemented in the FPGAs of the TMUs for the track matching.

The tracklets are transmitted in a fixed order with descending z -value, and, if several tracklets have identical z -values, with descending y . For a nominal vertex with a position uncertainty of ± 20 cm, only predefined combinations of padrows for the different layers can contribute to a track. Thus, only the projected y -coordinates for tracklets with consistent z -positions are compared in parallel instances. The y -coordinate is projected into the virtual plane via the deflection:

$$y_{\text{proj},i} = y_i + \frac{d_{y,i}}{d_x}(x_{\text{proj}} - x_i). \quad (2.1)$$

The deflection d_x denotes the fixed drift length of the chambers, x_i is taken from the radial position of the corresponding layer and x_{proj} is the fixed radial position of the projection layer.

At least four tracklets are required to form an on-line track and not more than one tracklet per layer can contribute to a track. Therefore, the on-line tracks consist of four to six tracklets.

2.5.3. Transverse momentum reconstruction

All tracks found by the TRD describe circular trajectories in the transverse plane because of the magnetic field in longitudinal direction. Since the bending radii for primary high- p_T tracks are large, a straight line fit is a justifiable approximation for high- p_T tracks (see Figure 2.8). By using several simplifications [28], the inverse transverse momentum of the tracks can be estimated from the offset a of the fit to the nominal vertex (see Figure 2.9) and a constant factor called $c1$:

$$p_{T,\text{GTU}} = \frac{c1}{a}. \quad (2.2)$$

The constant $c1$ takes into account, that the intersecting points of the straight line fit and the trajectory are not exactly known. They are estimated dependent on the

2. Transition Radiation Detector

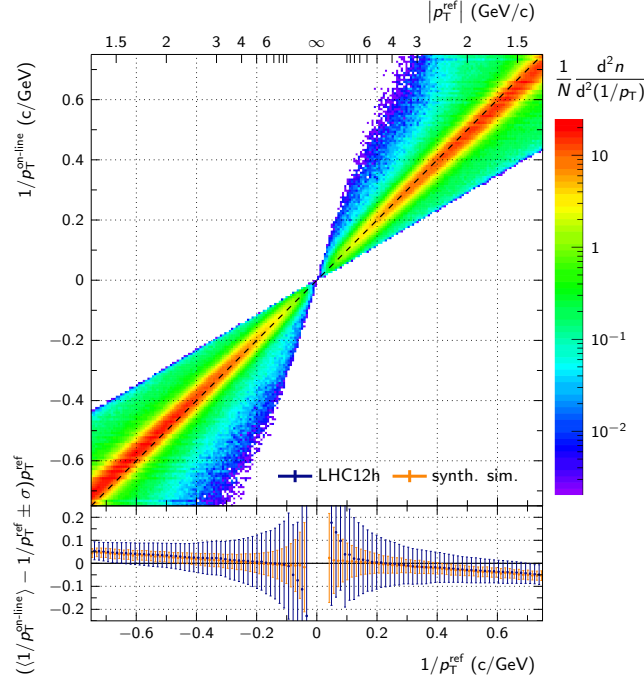


Figure 2.8.: Correlation between the fit parameter $a \propto p_T^{-1}$ to the off-line calculated p_T^{-1} [31].

layers contributing a tracklet to the track and stored in a look-up table for every possible combination of layers.

The drawback of the p_T reconstruction via a straight line fit is that it fails for on-line tracks which do not originate from the primary vertex but are matched to form a track nevertheless. This leads to the background of the late conversions in the triggers of the TRD (see Section 3.1). The results of the on-line tracking algorithm summarizing the above sections are shown in Figure 2.9.

2.6. TRD trigger contributions

As described in the above sections, the TRD is able to do fast standalone particle tracking on-line including p_T reconstruction and PID measurement. This feature allows the contribution of physics triggers at level-1. Data from the TRD is only available after the acquisition has been initiated by a level-0 trigger. For physics data taking the following triggers were used in Run 1:

HCO Trigger for cosmic particles, requiring at least one valid on-line track. During cosmic ray data taking, a level-0 signal from TOF initiates the readout of the TRD.

HJT Jet trigger. At least three tracks with $p_T > 3 \text{ GeV}/c$ are found in a single TRD stack. The η - φ area of one stack is comparable with the size of a typical jet cone.

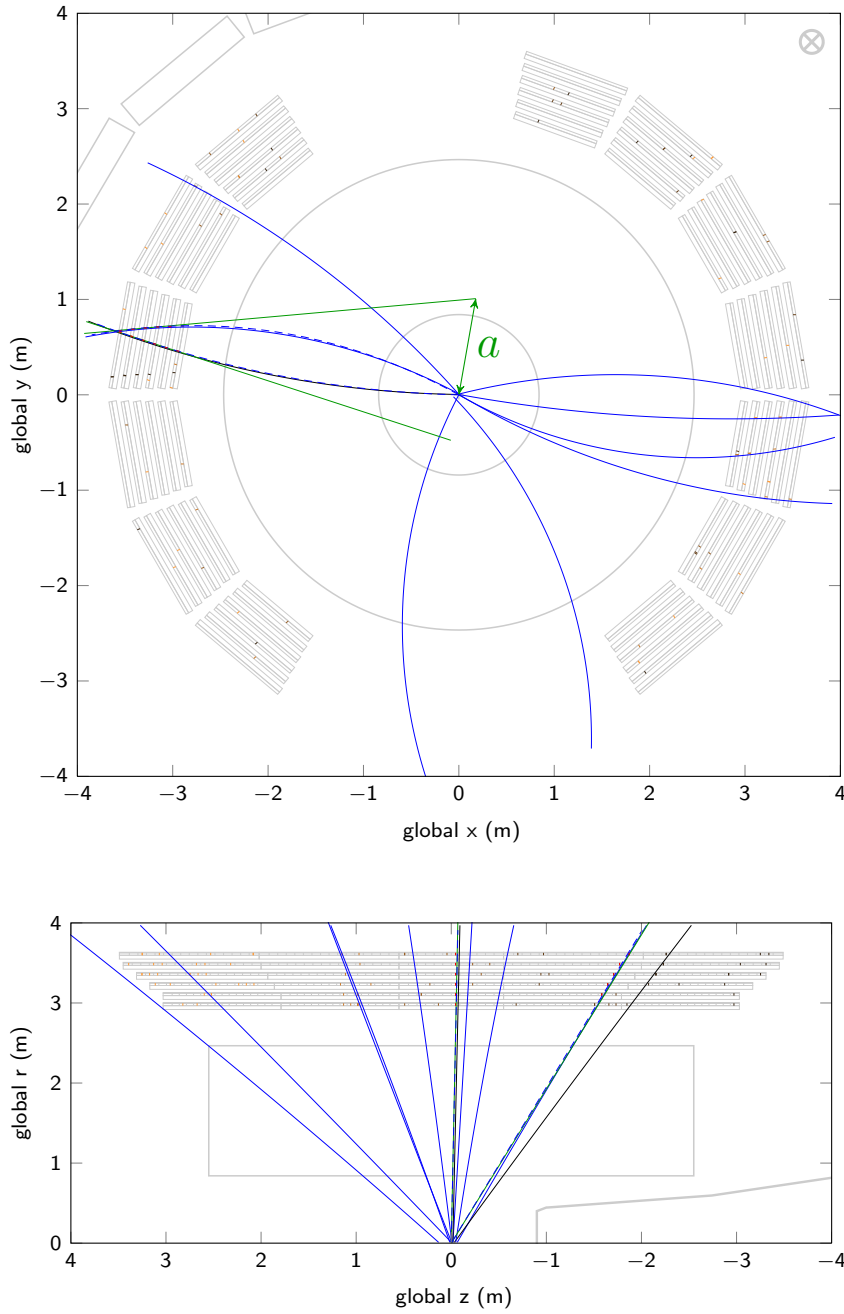


Figure 2.9.: Event display as seen by the TRD after on-line reconstruction together with global tracks from the off-line reconstruction (blue). Top: For tracklets which are matched to form a track, a straight line fit is performed (green) and the transverse momentum is taken from the offset of the fit to the nominal vertex position denoted as a . Global tracks crossing the boundaries of different detector stacks are not reconstructed on-line. Bottom: Only groups of tracklets (red) consistent with primary tracks are considered for matching in the longitudinal plane [26].

2. Transition Radiation Detector

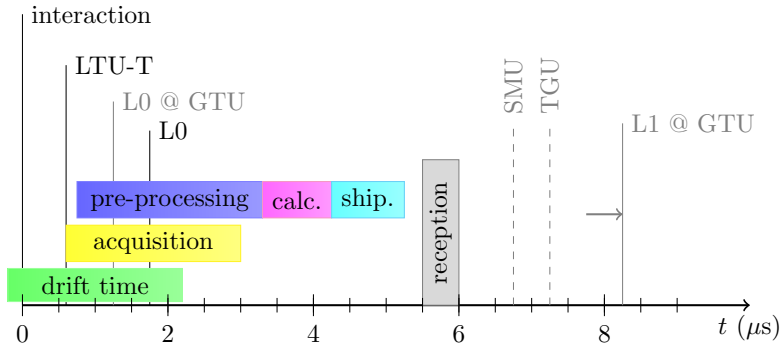


Figure 2.10.: Timing of the on-line tracking of the TRD. GTU relevant timings are shown in gray. The tracklet calculation in the front-end electronics must be initiated by a wake-up signal (LTU-T). The global tracking starts already with the shipment of the tracklets to the GTU. After the reception of all tracklets at about $6 \mu\text{s}$ after the interaction $\sim 1.5 \mu\text{s}$ remain for issuing a level-1 trigger. The time was increased by 500 ns for Run 2 to allow for the late conversion rejection. Adapted from [26].

HQU Quarkonia trigger. At least one track with $p_T > 2 \text{ GeV}/c$, a PID value above 164 and at least 5 tracklets with a tracklet in layer-0 is found.

HSE Heavy-flavor trigger. At least one track with $p_T > 3 \text{ GeV}/c$, a PID value above 144 and at least 5 tracklets with a tracklet in layer-0 is found.

HEE Heavy-flavor trigger with EMCAL acceptance (as of 2012/2013). The same requirements as for HSE, but the track needs to be found in either sector 6, 7 or 8.

Based on the large amount of information available for the on-line trigger decision, multiple other trigger contributions are conceivable. For example a selection of tracks with a very large energy deposit could be used to trigger on nuclei. Another example are two tracks found in opposite stacks of the detector with similar p_T . They could trigger on heavy-flavor decays for example from J/ψ . Limitations of the triggers contributions are merely the complexity of the required calculations and the available time for the trigger decision.

An overview for the timing of the trigger contribution of the TRD is given in Figure 2.10. After the GTU has received all tracklets from the FEE, about $1.5 \mu\text{s}$ remain for the level-1 trigger decision sent via the TGU to the CTP. The data shipment to DAQ is initiated by an level-1 accept signal from the CTP.

3. Late conversions

The following Chapter explains how the dominant background of the single electron triggers of the TRD, i.e. electrons from photon conversions in the material between TPC and TRD, can be rejected. Based on a proposal by Peter Glässel [32] and Uwe Westerhoff [30], the sagitta of the tracks inside the TRD can be used to distinguish on-line between electrons from the above mentioned conversions and electrons originating from the primary vertex. The tough timing constraint of 7 μs for the level-1 trigger decision with respect to a level-0 trigger signal puts high demands on the speed of the sagitta calculation.

First, the problem of the late conversions will be discussed in Section 3.1 and the rejection principle is presented in Section 3.2 and Section 3.3. Second, the implementation of the sagitta calculation for the TRD in software is described in Section 3.4, and last, a very simple algorithm that was implemented in the GTU is presented in Section 3.5.

3.1. Fake high- p_{T} tracks

In proximity of the Coulomb field of an atomic nucleus, photons can convert into an electron-positron pair. The nucleus has to absorb the recoil of the created particle pair:

$$\gamma + X \longrightarrow e^+ + e^- + X^*. \quad (3.1)$$

In this thesis, photon conversions at large radii will be referred to as *late conversions*. Late conversion occur mostly in the material in between the outer edge of the TPC and the first layer of the TRD. Comparatively rarely they also occur in the gas of the TPC. Particle tracks originating from the primary collision vertex are referred to as *primary tracks*.

The bending radius of the late conversions is small compared to primary tracks in the TRD. However, the tracklets of the late conversions might still be matched on-line to a track by the GTU, as their production vertex is very close to the inner radius of the TRD. Additionally, the straight line fit performed by the GTU to determine the transverse momentum of the particles (see Section 2.5) typically falsely points close to the primary collision vertex. In that case the on-line calculated transverse momentum will exceed the true p_{T} significantly.

An example of such a late conversion is shown in Figure 3.1. The transverse momentum of conversion leg A is calculated to be $p_{\text{T}}^{\text{on-line}} = -3.1 \text{ GeV}/c^1$. This exceeds the thresholds for all single electron triggers (compare Section 2.6). On the other hand, the

¹The on-line transverse momentum calculated by the GTU is signed. The sign depends on the side of the nominal vertex on which the straight line fit proceeds.

3. Late conversions

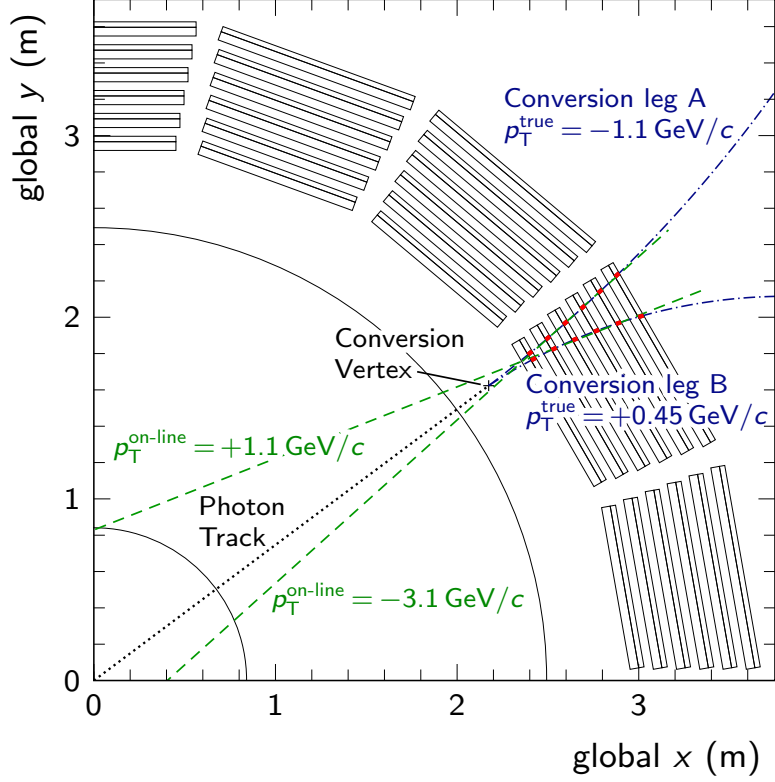


Figure 3.1.: A photon converts into an electron-positron pair in the supporting structure of TPC and TRD. The two low- p_T tracks from the conversion (drawn in blue) are found by the GTU. The straight line fit (drawn in green) overestimates the transverse momentum significantly, as it points close to the primary vertex at $(0, 0)$ [31].

true transverse momentum of the track determined via off-line reconstruction is only $p_T^{\text{true}} = -1.1 \text{ GeV}/c$. As late conversions traverse the TRD much more often than primary electrons, they pose a significant background for the single electron triggers of the detector.

In addition to a p_T threshold, an electron probability (PID value) above certain thresholds is required by the single electron triggers. A more stringent cut with respect to the reconstructed PID value is not feasible for the rejection of late conversions, since the conversion particles are real electrons².

To arrive at acceptable event rejection factors for the single electron triggers during LHC Run 1, the PID cut values had to be chosen rather high, resulting in an efficiency loss and possibly inducing systematic uncertainties for analyses. Furthermore, tracks without a contributing tracklet in the first layer of the TRD and tracks consisting of only four tracklets were ignored for the trigger decision. A higher number of tracklets within a track improves the overall performance of the reconstruction of track parameters. The requirement of a tracklet in the first layer rejects late conversions originating from in

²In this thesis, electron refers to both e^- and e^+ .

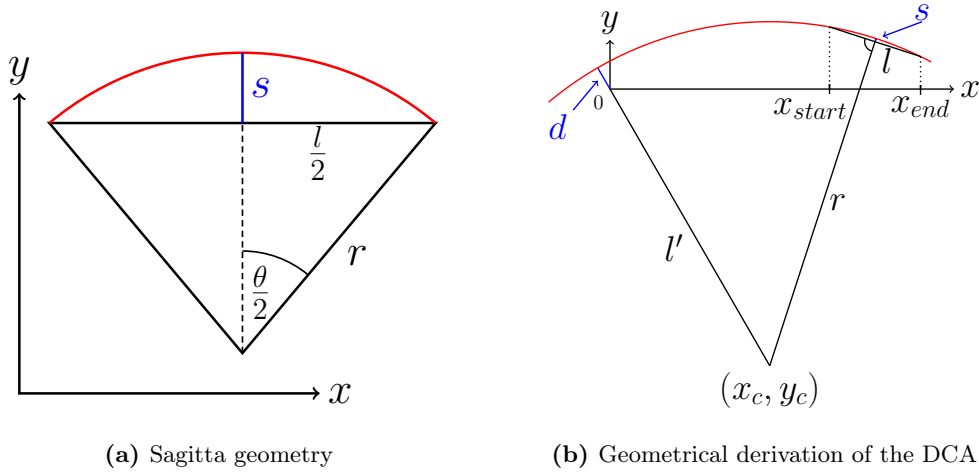


Figure 3.2.: The sagitta s is defined as the distance from the center of a circular arc to the center of its base l (a). For charged tracks that are bend by a magnetic field, s is proportional to p_T^{-1} and can be derived by using simple geometry. The sagitta can also be used to calculate the DCA d of a track (b).

between the active areas of the first layer and the second layer.

Still, the number of triggered events which did not contain a primary high- p_T track was above 90% for both the HQU trigger the HSE trigger. Requiring a matching primary track in the TPC for TRD tracks which fired the trigger was used to reject the events triggered by fake high- p_T tracks. Since electrons from late conversions are not matched to a TPC track which points to the primary vertex, they are rejected by this method.

However, the tracking information of the TPC is not available for the level-1 trigger decision, due to its large readout time. The clean-up of the triggered sample is hence only possible either in the HLT or during off-line reconstruction. The effective dead times of the TRD triggers thus increase from the level-1 latency to at least the latency for the availability of the tracking information of the TPC. For a reasonable application of the single electron triggers of the TRD, a different approach to reject late conversions is therefore needed.

3.2. Reconstruction of track parameters from sagitta

Late conversions pose a problem for the TRD triggers, since the on-line tracking algorithm performs a straight line fit to the found tracks under the assumption that the tracks originate from the primary vertex without taking their local curvature into account. A measurement of the local curvature will thus reveal a discrepancy with respect to the transverse momentum obtained via the straight line fit. This discrepancy shall be used to reject late conversions.

One possibility to determine the local curvature of a trajectory is the measurement of

3. Late conversions

its sagitta, defined as the distance from the center of a circular arc to the center of its base. In this section, the reconstruction of the transverse momentum and the determination of the Distance of Closest Approach (DCA) of the trajectory to the primary vertex, both from the sagitta, will be described.

As seen from Figure 3.2a, the sagitta s can be derived from the radius r of the circle and the opening angle θ of the circular arc [33]:

$$s = r - r \cos \frac{\theta}{2} = 2r \sin^2 \frac{\theta}{4}. \quad (3.2)$$

Using the small angle approximation for θ , which is feasible for large radii³, it follows that:

$$\frac{\theta}{2} \simeq \frac{l/2}{r} \Rightarrow \theta \simeq \frac{l}{r}. \quad (3.3)$$

Hence, putting together Equation (3.2) and Equation (3.3) and again applying the small angle approximation:

$$s \simeq \frac{l^2}{8r}. \quad (3.4)$$

The radius can be substituted by the transverse momentum using the well-known formula: $p_T(\text{GeV}/c) = 0.3 q(e) B(\text{T}) r(\text{m})$. The sagitta in meter is then given by:

$$s(\text{m}) \simeq \frac{0.3 q(e) l^2(\text{m}^2) B(\text{T})}{8 p_T(\text{GeV}/c)}. \quad (3.5)$$

Thus, the sagitta of a track is proportional to the inverse transverse momentum.

In addition to the calculation of the transverse momentum, the DCA can be determined via the sagitta and hence be used to identify late conversions. Its calculation is a little more complex, but also purely geometrical. The involved parameters are shown in Figure 3.2b. To determine the virtual center (x_c, y_c) of a circular trajectory one drops a perpendicular on the base of the circular arc l with the length $r - s$. Here, r is the radius of the circle and s its sagitta with respect to l .

In mathematical terms, using the abbreviation $\lambda = \frac{r-s}{l}$ and the coordinates $(x_{\text{start}}, y_{\text{start}})$ and $(x_{\text{end}}, y_{\text{end}})$ for the beginning and end of the base l , respectively, the virtual center of the trajectory is calculated as follows:

$$x_c = \frac{1}{2}(x_{\text{start}} + x_{\text{end}}) + \lambda (y_{\text{end}} - y_{\text{start}}), \quad (3.6)$$

$$y_c = \frac{1}{2}(y_{\text{start}} + y_{\text{end}}) + \lambda (x_{\text{start}} - x_{\text{end}}). \quad (3.7)$$

The distance l' of the virtual center of the trajectory to the nominal vertex at $(0, 0)$ is given by $l'^2 = x_c^2 + y_c^2$. Together with the radius $r \simeq \frac{\sqrt{l}}{8s}$ (Equation (3.4)) one finds for the DCA d :

$$d = r - l' = \frac{r^2 - l'^2}{r + l'} \approx \frac{r^2 - l'^2}{2r}. \quad (3.8)$$

³Although the radius of the late conversions is small compared to primary tracks, the small angle approximation is valid. Approximating $\sin \theta/2 \approx \theta/2$ results in a deviation of less than 0.2% for a track with $p_T = 0.5 \text{ GeV}/c$. This is negligible compared to the other uncertainties of the sagitta calculation with the TRD.

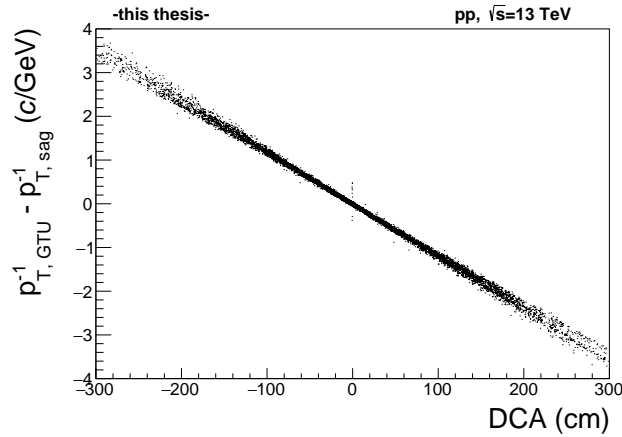


Figure 3.3.: The DCA is plotted versus the deviation of the inverse transverse momenta for all tracks with $p_T > 2 \text{ GeV}/c$ found on-line by the TRD (no PID selection). The correlation is clearly visible. Thus, cuts on these parameters yield similar results.

The last approximation takes into account, that r and l' are almost identical for primary tracks. Late conversions can thus be identified solely by their larger nominator in Equation (3.8).

3.3. Identification of late conversions

Distinguishing on-line between tracks from late conversions and primary tracks is possible by exploiting the local curvature of the tracks within the TRD. It is much higher for low- p_T tracks from late conversions than for high- p_T primary tracks. In the previous section it is shown that the local curvature can be determined by calculating the sagitta of the tracks. The sagitta in turn can be used to calculate p_T^{-1} or the DCA. Based on these parameters, there are two possibilities to identify late conversions. First, the inverse transverse momentum calculated via the sagitta is compared to the inverse transverse momentum determined by the straight line fit done by the GTU:

$$\Delta p_T^{-1} := |p_{T,GTU}^{-1} - p_{T,sag}^{-1}|. \quad (3.9)$$

For late conversions, a strong deviation is expected. Second, the DCA itself is evaluated, which is much larger for late conversions than for real primary tracks.

Since both the DCA and p_T^{-1} are determined via the sagitta of the tracks, Δp_T^{-1} and the DCA are correlated (see Figure 3.3). The difference between both methods is that late conversions can be directly identified from the DCA, whereas p_T^{-1} needs to be compared to the inverse transverse momentum calculated via the straight line fit.

On-line calculation of the DCA is much more costly in terms of computing time than determining the inverse transverse momentum via the sagitta. Even if the square root in the calculation of l is only approximated, three divisions are present which cannot be

3. Late conversions

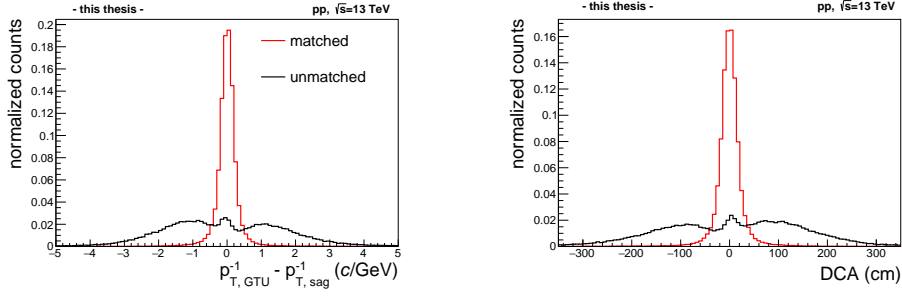


Figure 3.4.: The left plot shows the deviation in inverse momenta Δp_T^{-1} for TRD tracks with $p_T > 2$ GeV, the plot on the right shows their DCA distribution. All curves are normalized to the respective track counts. Tracks with a matching TPC track are drawn in red, whereas tracks without a matching TPC track are drawn in black. These tracks are most likely late conversions. The rejection of late conversions at a given efficiency for matched tracks agrees on the percent level.

done in parallel but have to be executed successively. One for λ , one for r and finally one for the DCA.

Both methods have been implemented in the software simulation of the GTU [27] (see Section 3.4.2). In Figure 3.4 the performance of the late conversion rejection is shown for a measurement of the DCA and Δp_T^{-1} , respectively. Both parameters are plotted for TRD tracks which are matched to a TPC tracks in the off-line reconstruction and for tracks without a matching track in the TPC. The unmatched tracks originate most likely from late conversions. The remaining unmatched tracks originate from matching inefficiencies of TPC to TRD tracks [31].

The resulting efficiencies for the identification of late conversions via Δp_T^{-1} and the DCA are very similar. Therefore, the comparison of the inverse momenta is chosen to identify tracks from late conversions due to the lower computational cost.

3.4. Sagitta calculation

Certain boundary conditions apply for the on-line calculation of the sagitta with the TRD. The particle trajectory is defined by the 4 to 6 tracklets resulting in a track. Figure 3.5 shows the schematics for a track consisting of 6 tracklets. Changes for tracks consisting of fewer tracklets will be discussed later.

To determine the sagitta, one has to calculate the area between the trajectory and its base A_S (light red area). In our case, the base is the distance between the first and the last found tracklet in the transverse plane. To obtain A_S , firstly the total area under the curve A_{tot} is evaluated. Using the trapezoidal rule for approximating definite integrals on a uniform grid [34]:

$$\int_a^b f(x) dx \approx \frac{h}{2} \sum_{k=0}^{N-1} (f(x_{k+1}) + f(x_k)) \quad (3.10)$$

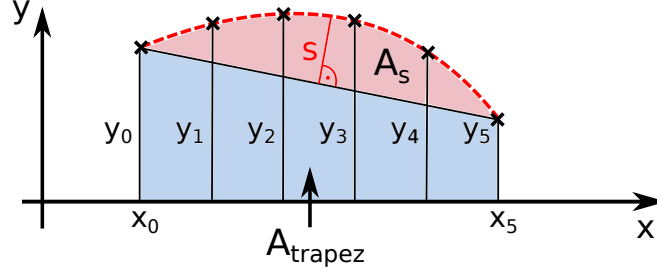


Figure 3.5.: Particle traversing a TRD stack. The sagitta s (red solid line) can be approximated using the y -coordinates of the tracklets together with the x -coordinates given by the geometry of the detector. The bending of the curve is strongly exaggerated to make the sagitta visible. For example an electron with $p_T = 3 \text{ GeV}/c$ and a path length of $l = x_5 - x_0 = 63 \text{ cm}$ in a homogeneous magnetic field of $B = 0.5 \text{ T}$ has a sagitta of $s \approx 2.5 \text{ mm}$.

with grid spacing $h = \frac{b-a}{N}$ and N equally spaced segments, one can approximate the total area under the curve. For a track with contributing tracklets in each layer one has $N = 5$ segments and a spacing of $h = \frac{x_5 - x_0}{5} = \Delta x$, where Δx denotes the radial distance between the readout pads of two consecutive layers.

It follows that:

$$A_{\text{tot}} = A_S + A_{\text{trapez}} \approx \frac{\Delta x}{2} (y(x_0) + 2y(x_1) + 2y(x_2) + 2y(x_3) + 2y(x_4) + y(x_5)). \quad (3.11)$$

The area of the trapezoid (light blue area) is given by:

$$A_{\text{trapez}} = \frac{5\Delta x}{2} (y(x_0) + y(x_5)). \quad (3.12)$$

Subtracting Equation (3.12) from Equation (3.11) and using the abbreviations $y_i := y(x_i)$ one obtains:

$$A_S = \frac{\Delta x}{2} (-4y_0 + 2y_1 + 2y_2 + 2y_3 + 2y_4 - 4y_5). \quad (3.13)$$

The sagitta can be approximated with the assumption of a parabolic circle segment:

$$s \approx \frac{3}{2} \frac{A_S}{l}. \quad (3.14)$$

In the formula above, $l = \sqrt{(x_5 - x_0)^2 + (y_5 - y_0)^2}$ is the distance between the first and last tracklet of the track.

3. Late conversions

Combining Equation (3.14) and Equation (3.13) and inserting them in Equation (3.5) leads to p_{T}^{-1} :

$$p_{\text{T},\text{sag}}^{-1} = \frac{6 \Delta x}{0.3 qBl^3} (-4y_0 + 2y_1 + 2y_2 + 2y_3 + 2y_4 - 4y_5). \quad (3.15)$$

At this point, only the length of the track inside the TRD l and the y -values of the tracklets depend on the event. The other parameters are constant and can thus be pre-calculated. The factors in front of the respective y -values depend on the tracklet composition of the track. They are referred to as *prefactors* (see next paragraph). Especially the calculation of l is expensive with respect to the computing time, as a square root needs to be evaluated. To be able to calculate p_{T}^{-1} within the time available for the level-1 trigger decision, a further simplification of the calculation will be described in Section 3.4.1.

Treating missing layers

The tracking efficiency and acceptance of the detector is not perfect. Losses in efficiency and acceptance originate e.g. from stack boundaries and dead chambers. Therefore, some tracks might consist of only four or five tracklets, respectively. A lower number of tracklets does not form an on-line track (see Section 2.5.2). For the tracks with missing layers the approximation of A_{S} has to be adjusted.

In Equation (3.13) the prefactors for layer i are set to zero, if no contributing tracklet for layer i can be found. For missing tracklets in middle layers this is compensated by increasing the prefactors of the neighboring tracklets in layers $i - 1$ and $i + 1$ by one. If a second not adjacent layer does not contribute a tracklet to the track this procedure is repeated. In case of an adjacent missing layer the prefactors of the adjacent layers which contribute a tracklet are increased by two.

If a tracklet in the first or last layer is missing, the number of segments for calculating the area A_{S} with the trapezoidal rule decreases, which also results in different prefactors for the other layers. An overview of the prefactors depending on the layers which contribute a tracklet to the track is given in Table 3.1. The condition of the on-line tracks to consist of either 4, 5 or 6 tracklets, results in $\binom{6}{4} + \binom{6}{5} + 1 = 22$ possible layer compositions for an on-line track.

Cut on Δp_{T}^{-1}

The GTU does not compute p_{T} by default. If the trigger conditions require only tracks above a certain p_{T} -threshold, the parameter a obtained by the straight line fit can directly be compared to a threshold (see Section 2.5.3) [28].

In the new implementation of the on-line tracking algorithm, the division remains unnecessary for the trigger calculation, as the *inverse* transverse momenta shall be compared. Thus, to obtain p_{T}^{-1} from the straight line fit, a needs to be multiplied with the inverse of the constant c_1 (compare Equation (2.2)):

$$p_{\text{T},\text{GTU}}^{-1} = c_1^{-1}(m) \cdot a \quad (3.16)$$

tracklet mask	prefactors for layer i					
	$i = 0$	1	2	3	4	5
111111 ₂	-4	2	2	2	2	-4
111110 ₂	0	-3	2	2	2	-3
111101 ₂	-3	0	3	2	2	-4
111011 ₂	-4	3	0	3	2	-4
110111 ₂	-4	2	3	0	3	-4
101111 ₂	-4	2	2	3	0	-3
011111 ₂	-3	2	2	2	-3	0
111100 ₂	0	0	-2	2	2	-2
111010 ₂	0	-2	0	3	2	-3
101110 ₂	0	-3	3	0	3	-3
101110 ₂	0	-3	-2	3	0	-2
011110 ₂	0	-2	2	2	-2	0
111001 ₂	-2	0	0	4	2	-4
110101 ₂	-3	0	4	0	3	-4
101101 ₂	-3	0	3	3	0	-3
011101 ₂	-2	0	3	2	-3	0
110011 ₂	-4	4	0	0	4	-4
101011 ₂	-4	3	0	4	0	-3
011011 ₂	-3	3	0	3	-3	0
100111 ₂	-4	2	4	0	0	-2
010111 ₂	-3	2	3	0	-2	0
001111 ₂	-2	2	2	-2	0	0

Table 3.1.: Overview of the prefactors for the sagitta calculation depending on the layers contributing tracklets to the track. The tracklet mask is a bit vector specifying the contributing layers. The most significant bit corresponds to the outermost layer.

3. Late conversions

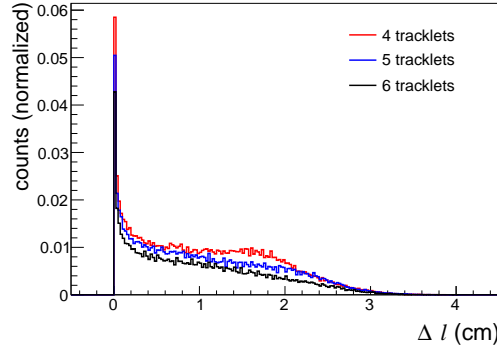


Figure 3.6.: The above plot shows the deviation of the track length inside the TRD for the exact length and the approximated length ($\Delta l = l_{\text{exact}} - l_{\text{approx}}$). The tracks are a sample of $\sim 2.5 \cdot 10^5$ tracks from 2015 pp data without any selective cuts.

The 22 values $c_1^{-1}(m)$ (m denotes the tracklet mask) can be pre-calculated and stored in a look-up table. To filter out tracks from late conversions, a cut on the difference of the inverse transverse momenta derived from the straight line fit and the sagitta method, respectively, is introduced:

$$\Delta p_T^{-1} = |p_{T,\text{GTU}}^{-1} - p_{T,\text{sag}}^{-1}| \leq \text{threshold}. \quad (3.17)$$

Tracks for which the above equation holds are marked as primary tracks.

3.4.1. Simplification

Due to the orientation of the detector modules towards the interaction point, the length of a track inside the TRD is primarily covered in the direction of x (in local detector coordinates). This leads to the idea to approximate the length solely by the distance covered in x :

$$l \approx k \Delta x \quad (3.18)$$

With $k = 3, 4$ or 5 , depending on the layer where the first and the last tracklet of the tracks is found, respectively.

Using Equation (3.18) in case of a track consisting of 6 tracklets, Equation (3.15) simplifies to:

$$p_{T,\text{sag}}^{-1} = \frac{6}{0.3 k^3 \Delta x^2 B} (-4y_0 + 2y_1 + 2y_2 + 2y_3 + 2y_4 - 4y_5). \quad (3.19)$$

At this point the complete fraction can be calculated in advance for the three different values of k , so that only the y -components of the track have to be summed up accordingly with the respective prefactors. This can be done within the timing constraint of the level-1 trigger.

The deviation of the approximated track length in the TRD with respect to the exact calculated length can be seen in Figure 3.6. The absolute length of a track inside the

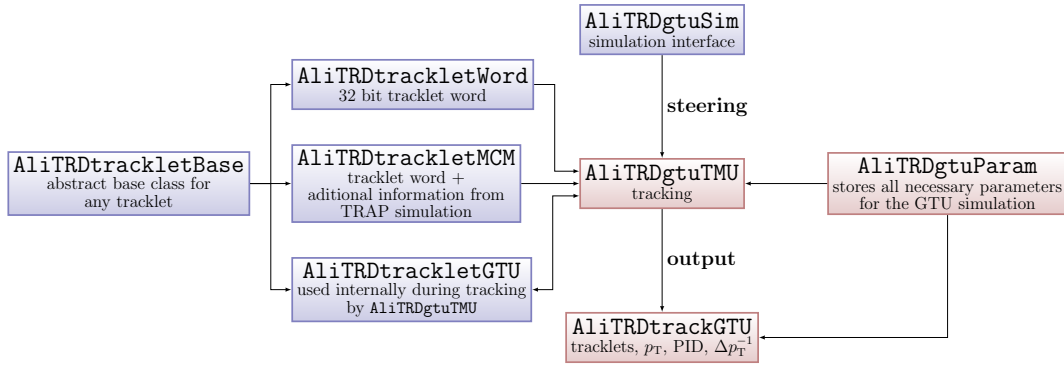


Figure 3.7.: Important classes for the GTU simulation in the AliRoot off-line framework. The sagitta calculation is implemented in `AliTRDgtuTMU`. The required look-up tables and parameters are stored in `AliTRDgtuParam`. The result is stored in the produced tracks.

TRD varies between 37.8 cm and ~ 70 cm, depending on the number of found tracklets and the curvature of the track. Assuming the smallest possible values for l_{exact} , the fraction of tracks consisting of 5 or more tracklets with $\Delta l/l_{\text{exact}} < 0.04$ is over 90%. The most accurate calculation of p_T^{-1} via the sagitta depends on the third power of the length, therefore the relative error is $\Delta p_T^{-1}/p_T^{-1} \leq 0.12$.

Note, that the figure of merit is not a precise reconstruction of the inverse transverse momentum of all tracks on-line, but the rejection of late conversions by their deviation of the inverse transverse momenta. As the simplification, next to two additions and a multiplication, saves the approximation of a square root, which would also introduce an error for the length and be very costly in terms of computing time, the simplification is justified.

3.4.2. Implementation in AliRoot GTU simulation

This section describes the implementation of the late conversion rejection into the software simulation of the GTU.

The simulation for the on-line tracking has been implemented as an algorithm in the same way as in the on-line electronics [27], combining tracklets to tracks and calculating their track parameters, e.g. p_T and PID. It is fully integrated into the ROOT-based [35] AliRoot off-line framework [36], used for reconstruction, simulation and analysis of data with ALICE. The simulation can be done for Monte Carlo data, Event Summary Data (ESD) or individual tracklet files for debugging and testing purposes.

An overview of the GTU simulation framework is given in Figure 3.7. A more detailed description can be found in [27]. The class `AliTRDgtuSim` starts the simulation, loads necessary tracklets and forwards the output. The major tasks are done by the class `AliTRDgtuTMU`. Here, the track matching and reconstruction is done stack-wise. Since the information stored in a tracklet depends on the input of the simulation, different tracklet classes can serve as input for `AliTRDgtuTMU`. The class `AliTRDtrackGTU` is used

3. Late conversions

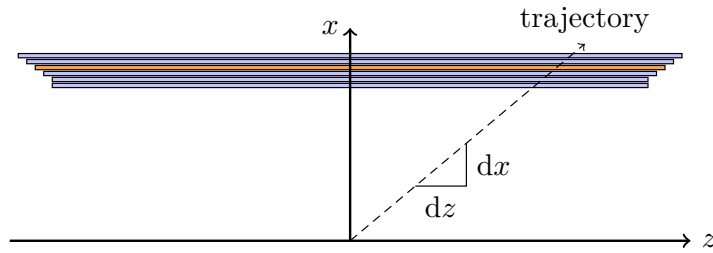


Figure 3.8.: The pad-tilting correction is done by a straight line fit from the primary vertex at (0,0) to the z -position of the pad in the reference layer (orange). The slope is used to obtain the z -position for the other layers.

as output for the reconstructed tracks. They can either be added to the event or written to an extra file. The latter is useful for comparison to results obtained in hardware (see Section 4.1). All necessary parameters are stored in the designated class `AliTRDgtuParam`.

For the sagitta calculation and the rejection of late conversions, the classes `AliTRDgtuTMU` and `AliTRDtrackGTU` were adapted. The routine for the reconstruction of the track parameters now additionally determines the sagitta and the deviation of the inverse transverse momenta and adds the information to the track.

The look-up tables and parameters are added to the parameter class. The implementation is oriented on the hardware implementation described in Section 3.5.

As the FPGAs in the GTU use fixed-point arithmetic, only integer calculations are used in the software simulation as well. Numbers with decimal places are shifted by a constant factor of 10^6 . When this factor is applied, no deterioration of the result compared to floating-point calculation was detected.

3.4.3. Possible optimizations

Different possibilities to optimize the sagitta calculation as proposed in [30] are implemented in the AliRoot simulation of the GTU. The optimizations are adapted from the off-line reconstruction and simplified in order to meet the latency requirements.

Alignment correction accounts for misalignment of the TRD chambers within one stack. The measured y -component of a tracklet is shifted by a constant value dependent on the chamber where the tracklet is found. At the moment the values are stored in a look-up table of the class `AliTRDgtuParam`. After the commissioning, each MCM will store the relevant correction value for its chamber and the correction will be done locally before the tracklets are shipped to the GTU.

Pad-tilting correction: The tilting of the pads by β_{tilt} improves the z -resolution at the cost of a slight deterioration in the y -position measurement. A simple approach can be

missing layer	layer to be removed
0	5
1	4
2	1
3	4
4	1
5	0

Table 3.2.: One additional tracklet is artificially removed in case a track consisting of 5 tracklets is found. The layer to be removed is tilted in the opposite direction of the missing layer.

used to correct y on-line⁴ for the tilted pads and thus improve the sagitta calculation.

On-line, only the information of the pad number determines the z -position. The pad-tilting correction performs a straight line fit in the x - z -plane from the primary vertex to a tracklet in a chosen reference layer⁵ to calculate the z -position of the tracklet in layer i of the track (see Figure 3.8). The differences of the calculated z -positions z_{fit} and the known z -positions z_{row} of the pad provide the correction for the y -position of the tracklets:

$$y_{\text{corr},i} = (z_{\text{row},i} - z_{\text{fit},i}) \cdot (\pm \tan \beta_{\text{tilt}}). \quad (3.20)$$

Artificial tracklet removal: The tilting of the pads has another effect on the sagitta calculation for tracks with missing tracklets. If one tracklet is missing, the deterioration in y will become asymmetric, as the same number of pads is tilted left and right. To prevent this, an additional tracklet is artificially removed in case of a track consisting of 5 tracklets. The tracklet is removed in a layer tilted in the opposite direction of the layer with the missing tracklet. Technically, this is trivial, as the prefactors for the correspondent hit masks can easily be adapted. The tracklets which are to be removed are listed in Table 3.2.

The optimization methods described above do not lead to a significant enhancement of the late conversion rejection performance as it is implemented in the hardware now (see Appendix A.2). Only if the length is not strongly simplified as described in Section 3.4.1, but the the distance of the track covered in y taken into account, possibly by approximating the square root, a stronger effect is visible [30]. On the other hand, this also leads to a more complicated algorithm and it is not clear, if the available computation time would suffice. Thus, for the implementation in hardware the most basic algorithm without further optimizations was chosen to allow for commissioning in sufficient time to activate the late conversion rejection during data taking at the end of 2015 (see Section 4.3).

However, the presented optimization methods are available for testing purposes in the AliRoot GTU simulation (disabled by default).

⁴In off-line reconstruction the y position is corrected by a more sophisticated algorithm [25].

⁵The default reference layer is layer 3. If the tracklet in this layer is missing, layer 4 is chosen. If there is no tracklet in both of these layers, the reference will be the layer 2.

3.5. Proposal for hardware implementation

The calculations introduced in this chapter are the basis for the implementation in the FPGA arrays of the GTU. The actual implementation in hardware as a combination of arithmetic operations and accesses to look-up tables is performed by Felix Rettig [31].

In software, the bit width for integer values is fixed, e.g. to 32 bit for the standard ROOT type `Int_t`. For the calculations in the FPGAs, the bit width of the signals and the values in the look-up tables are determined individually. They should occupy only the computing capacity which is necessary in order to keep the precision as in software.

Figure 3.9 shows the proposed architecture adaptation for the reconstruction units of the track matching units. It was used as a template for the hardware implementation. For a detailed description of the original architecture see [28].

The goal is to identify late conversions by their large deviation of the inverse transverse momenta. First, Equation (3.19) needs to be evaluated to determine $p_{T,\text{sag}}^{-1}$. Second, $p_{T,\text{GTU}}^{-1}$ is calculated and the absolute value of the deviation of both transverse momenta Δp_T^{-1} is compared to a threshold.

As shown in the previous sections, the calculation of $p_{T,\text{sag}}^{-1}$ depends on the tracklet composition of the track. Since only 22 possibilities exist for the 6 bit tracklet mask, it is translated into a 5 bit code number called `mask_id`. This code number is propagated to the look-up tables for the `prefactors` p_i and the `length_norm` l_{norm} to obtain the required values. Thus, Equation (3.19) is implemented as follows:

$$p_{T,\text{sag}}^{-1} = l_{\text{norm}} \cdot (p_0 y_0 + p_1 y_1 + p_2 y_2 + p_3 y_3 + p_4 y_4 + p_5 y_5). \quad (3.21)$$

Note, that l_{norm} and p_i depend on the `mask_id`. The prefactors range from -4 to 4. Hence, they require a precision of 4 bits. The matched tracks contain pointers to their contributing tracklets. These are stored in the memory of the input units. The binary values for the y -positions of the tracklets `yBin` are taken directly from the 32 bit tracklet word and have a precision of 13 bit.

In the first stages 1A and 1B the products of the prefactors and the binary values y_i are calculated and summed. For these operations a precision of 18 bits is sufficient. To obtain the inverse transverse momentum in stage 2, the normalization l_{norm} depending only on the number of layers k between the first and the last layer is necessary. It is scaled as in software

$$\text{length_norm}(\text{mask_id}) := 10^6 \cdot \frac{6}{0.3 k^3 \Delta x^2 B} \cdot 160 \mu\text{m} \quad (3.22)$$

and stored as a 15 bit signed integer. The last term accounts for the granularity of y_i in the tracklet word. Thus, $p_{T,\text{sag}}^{-1}$ is given in $10^{-6}(\text{GeV}/c)^{-1}$.

For the multiplication of `length_norm` with the sum of the products $p_i \cdot y_i$ a precision of 24 bit is estimated. During the commissioning an overflow of $p_{T,\text{sag}}^{-1}$ has been observed in rare cases. For details see Section 4.3.

At this stage the parameter `a` from the straight line fit is available as a 16 bit signed integer. A multiplication by the constant c_1^{-1} , defined as

$$c_1^{-1}(\text{mask_id}) := 10^6 \cdot \frac{1}{-c_1(\text{mask_id})}, \quad (3.23)$$

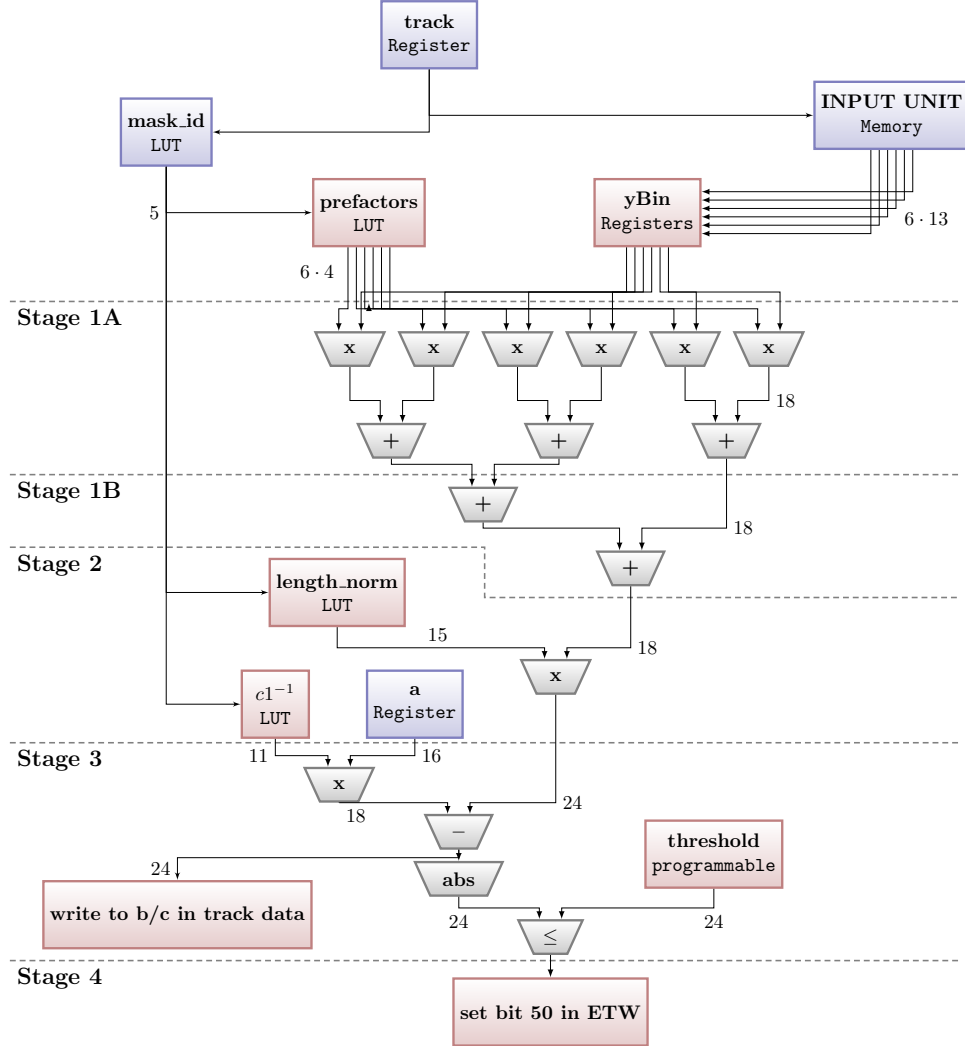


Figure 3.9.: Proposed and implemented algorithm for the late conversion rejection. Marked in blue is the infrastructure already available in the original design. p_{\perp}^{-1} can be calculated to a large extent in parallel from the tracklet y -values and the prefactors and a multiplication with `length_norm`. It is compared to p_{\perp}^{-1} calculated from the straight line fit and a flag is raised in case Δp_{\perp}^{-1} is below the programmable `threshold`. The bit sizes of the variables are indicated. A small x denotes a multiplication, + and - denote additions.

3. Late conversions

and stored as 11 bit integer in a look-up table, yields $p_{\text{T,GTU}}^{-1}$ in the same unit as $p_{\text{T,sag}}^{-1}$. All look-up tables for the late conversion rejection are shown in Table 3.3.

The absolute value of the difference of both inverse transverse momenta is compared to a configurable 22 bit **threshold** in stage 3 and a flag is set for particles, for which the equation

$$|p_{\text{T,GTU}}^{-1} - p_{\text{T,sag}}^{-1}| \leq \text{threshold} \quad (3.24)$$

holds.

In stage 4 the resulting flag is written to the Extended Track Word (ETW), which is a 64 bit integer representation of the track in the supermodule unit. The ETW contains the y -position of the track, references to the contributing tracklets and different flags needed for the calculation of the trigger signal. With the new design of the reconstruction unit, one bit is chosen to store the flag for the late conversion rejection. If this flag for a track is zero, the track can be ignored for the trigger decision.

A three dimensional linear regression was foreseen for the on-line tracking algorithm [28]. But at the moment only a one dimensional regression is performed resulting in the track parameter **a**. Since 30 bits of space in the track word are reserved for the other two fit parameters **b** and **c** but not used at the moment, this space is employed to store the inverse p_{T} deviation before the absolute value is taken. This allows for a simple comparison of the results in hardware to the results of the software simulation and in addition to verify the correct setting of the flag for a given Δp_{T}^{-1} .

In the following chapters the commissioning process as well as the resulting performance will be discussed.

3.5. Proposal for hardware implementation

hit mask	mask_id	length_norm ($10^6 \text{GeV}/c$) ⁻¹	$c1^{-1}$
111100	0	-14930	421
111010	1	-6298	404
110110	2	-6298	404
101110	3	-6298	404
011110	4	-14930	390
111110	5	-6298	408
111001	6	-3224	387
110101	7	-3224	387
101101	8	-3224	387
011101	9	-6298	374
111101	10	-3224	391
110011	11	-3224	387
101011	12	-3224	387
011011	13	-6298	374
111011	14	-3224	391
100111	15	-3224	387
010111	16	-6298	374
110111	17	-3224	391
001111	18	-14930	361
101111	19	-3224	391
011111	20	-6298	378
111111	21	-3224	396

Table 3.3.: The above values are stored in the look-up tables of both the AliRoot simulation and the hardware design. The corresponding prefactors are written in Section 3.4.

4. Commissioning

This chapter describes the commissioning of the hardware implementation of the late conversion rejection in the Global Tracking Unit (GTU). The goal is to ensure that the hardware implementation functions and that the calculations performed in hardware (resulting in Δp_T^{-1} and the corresponding flag) agree with the software simulation. After successful verification, the software simulation can be employed to analyse recorded data and evaluate the performance of the late conversion rejection.

The first step comprises tests with the hardware emulation of the GTU with the new FPGA designs and is described in Section 4.1. The tests are successfully passed for a small test sample of tracks.

Subsequent stability tests employing a GTU test setup in Heidelberg are performed to ensure that the raw data readout is not affected by the new designs.

After the stability tests are passed, the late conversion rejection is activated during data taking at the experiment with the results presented in Section 4.3. The on-line tracking algorithm is performed by the TRD, even if it is not contributing to the level-1 trigger. The resulting tracks are added to the ESD. Thus, by re-running the software simulation of the GTU for the ESD files, the hardware calculation can be verified.

4.1. Hardware simulation with ModelSim

A full simulation of the hardware tracking written in VHDL [37, 26, 31, 38] can be used to emulate the GTU hardware designs with ModelSim. For the first commissioning of the late conversion rejection, the hardware emulation is compared to the AliRoot simulation (see Section 3.4.2).

Both the hardware emulation and the software simulation perform stack-wise matching for provided tracklets from specific files and the parameters of the resulting tracks, i.e. p_T , PID value and additionally Δp_T^{-1} are calculated and written to an output file. The results for the calculation of Δp_T^{-1} should be equivalent on the bit-level as it is for the other track parameters [39].

A manual explaining the ModelSim procedure written by Sean Pennef is extended with information on debugging and the loading of individual tracklet files. It is added in the form of a \TeX document to the software repository of the GTU.

As mentioned above, the basic infrastructure for the tests is already available. Tracklet files in a special format are created with additional debug information to monitor the calculations in all stages of the reconstruction unit.

4. Commissioning

bit position	parameter (old)	parameter (new)
63..62		revision number
61..56		hit mask
55..38		fit offset a
37..33		unused
32	b	conversion flag
31..20		Δp_T^{-1} (first half)
19..8	c	Δp_T^{-1} (second half)
7..0		PID

Table 4.1.: The 64 bit track word is used to store the track reconstruction parameters. In the original design a 3-dimensional linear regression was foreseen with additional parameters b and c . These are used to store the conversion flag (in b) and Δp_T^{-1} (12 bits in b , 12 bits in c). Some bits of b remain unused.

4.1.1. Tracklet files

For the verification of the hardware implementation, it is important to cover all different tracklet compositions (tracklet masks) of the tracks. Thus, all entries in the look-up tables, which are dependent on the tracklet mask, are verified. Furthermore, all calculations are executed with the two's complement for signed integers. Thus, tracks with different charge must be tested as well.

To achieve this, tracks are selected from real data covering all different types with respect to charge, momentum, number of tracklets and production vertex and their composing tracklets are written to separate files in the required ASCII format (an example for such a tracklet file is given in Appendix A.3).

The individual creation of tracklet files is necessary because the hardware simulation is computationally intensive. The reconstruction of about 100 tracks takes approximately twelve hours. Therefore, ModelSim can be used to verify the tracking for individual tracks, but stress tests with sufficient statistics have to be performed with the actual GTU to verify the hardware implementation.

4.1.2. Tracking output

The tracks resulting from the simulations are written to a log file with their information stored in form of a 64 bit track word. Its content is shown in Table 4.1.

In the original design, it was foreseen to perform a 3-dimensional linear regression for the reconstruction of the tracks. Two parameters were introduced to store the resulting slopes with a precision of 12 and 18 bit, respectively. This unoccupied space in the track word is now used to store Δp_T^{-1} and the corresponding flag. Since Δp_T^{-1} has a precision of 24 bit, the least significant 12 bit of Δp_T^{-1} are stored in one parameter (named c), while the most significant 12 bit and the conversion flag are stored in the other parameter (named b) of the track word.

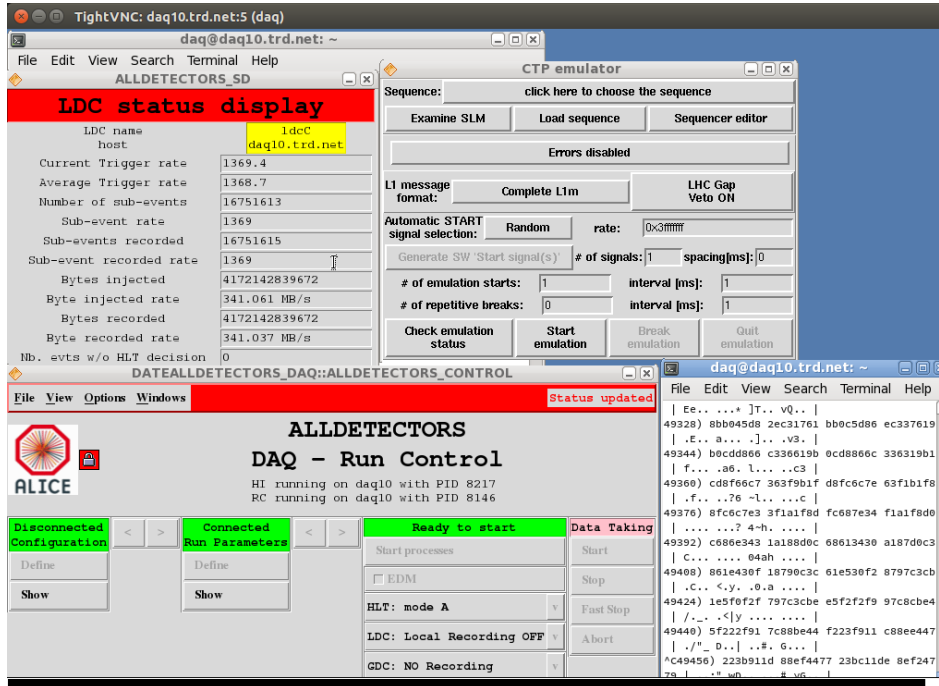


Figure 4.1.: Virtual network connection to the DAQ server of the GTU test setup in Heidelberg. Different trigger sequences are generated by the CTP emulator and an on-line checker tool is used to monitor the raw data stream.

4.1.3. Results

The first hardware design provided results for Δp_T^{-1} in agreement with the software simulation for about 100 of 126 tracks, which were taken as a test sample. The error in the hardware simulation was found by sorting the tracks according to their tracklet masks: All tracks with differing results consisted of only four tracklets in consecutive layers. The normalization factor for the length of the track `length_norm` is largest for these tracks (see Table 3.3). In the first proposal of the hardware implementation 14 bit were considered sufficient for the maximum value of `length_norm`. But as the look-up table consists of signed integer variables it has to be assigned with a 15 bit precision.

The fact that all values for `length_norm` are negative is then exploited by the compiler. Only variable bits are implemented into the look-up table, resulting in an effective occupation of 14 bit per entry.

After the correction, the results for the test sample of tracks from the ModelSim emulation and from the software simulation agree on the bit-level.

4.2. GTU test setup in Heidelberg

Before the new designs for the GTU are ready to be used during data taking, it has to be guaranteed that the raw data readout of the TRD is not affected, since the raw data

4. Commissioning

also passes through the FPGAs of the TMUs. A test setup consisting of 5 TMUs and 1 SMU is available in Heidelberg. At the moment there is no TRD chamber connected for signal generation, but the TMUs embody internal pattern generators, which can be used to generate either random pattern signals or pre-defined tracklets as input for the tracking logic [38]. The SMU is connected to a DAQ server, thus the full readout chain from the TMUs to the DAQ system can be tested.

To perform the long-term stability tests, the following steps are required: First, the hardware design used for the ModelSim simulation is compiled for the FPGAs of the TMUs and transferred to the DCS¹ boards of the test setup. The new design is now ready to be loaded onto the chips. Second, the data acquisition is started in parallel with an on-line checker tool [38] to verify the data integrity. Last, a CTP emulator is started to generate level-0 triggers at a constant rate of 40 MHz, equal to the clock frequency of the FPGAs. Thus, as soon as the tracking is finished and the busy flag is cleared, the readout and tracking continually starts again.

The test setup is steered via the DAQ machine, which in turn is connected to the TRD network in Heidelberg. The login is possible via a virtual network connection. A screen-shot of the virtual desktop is shown in Figure 4.1.

During continuous data taking over several days, no errors in the raw data stream were visible. Therefore, the designs were ready to be loaded for actual data taking with the detector.

4.3. Results in Pb–Pb data taking

After successful commissioning, the late conversion rejection was active during data taking twice in the 2015 Pb–Pb running period. Additional short standalone runs were taken with the TRD in each case in between fills and the raw data streams were inspected as a final test.

The late conversion rejection was first active at the end of fill 4681 for the last two runs². Part of the raw data was transferred to the computing farm of the GSI for further analysis. About $3 \cdot 10^3$ events were reconstructed which contained $45 \cdot 10^3$ on-line reconstructed tracks from the GTU. The comparison to the AliRoot simulation revealed a typing error in the look-up table of the prefactors which was easily fixed. Furthermore, for 11 tracks out of the sample 24 bit was not sufficient for Δp_T^{-1} and an overflow occurred. As a result the flag falsely indicated a track not originating from a late conversion. The probability of an overflow is as low as 0.02%, but this should be corrected for in the hardware implementation nevertheless. For covering all tracks, three additional bits are needed.

So far, only the design of the TMU was changed. But in order to propagate the flag from the late conversion rejection into the extended track word, an additional adjustment in the design of the SMU was necessary.

¹Detector Control System

²At ALICE, a run depicts a data taking period within one fill where the trigger clusters are constant.

fill	run number	comment
4681	245785, 245793	wrong look-up table entry
4719	246927, 246928, 246929, 246930 246937, 246942, 246944, 246945 246946, 246947, 246948, 246949	

Table 4.2.: This table lists the runs for which the late conversion rejection was active in the 2015 Pb–Pb data taking period.

Further stability tests with the new designs for both TMU and SMU, including at this point also the propagation of the flag to the extended track word, were passed successfully. Afterwards, the late conversion rejection was active for all runs of fill 4719, which was one of the last fills of the Pb–Pb data taking in 2015 before the winter shutdown. The runs for which the late conversion rejection was active are listed in Table 4.2.

No global reconstruction of these runs was available before the submission of this thesis, but the correct setting of the flag in the SMU is detected in the raw data stream.

Hence, the hardware implementation is verified to provide bit equivalent results compared to the simulation. The overflow is taken into account for the simulation as well: Only the 24 least significant bits of Δp_{T}^{-1} are propagated, higher bits are cut. The flag is not considered for the performance evaluation, instead, the resulting Δp_{T}^{-1} is compared to different thresholds.

Comparison to simulation results

The verification of the hardware implementation for reconstructed events can be done automatically. The analysis task `AliAnalysisTaskTRDgtuSim`, available in AliPhysics, is extended to additionally compare the outputs of the late conversion rejection.

The task needs to be configured to write the results of the sagitta calculation from the GTU simulation to the track word as it is done in hardware (see Table 4.1):

```
AliTRDgtuParam::WriteSagittaOutputToTrackWordBC(kTRUE)
```

Two histograms are filled with the individual deviations for the two parameters b and c (see Section 4.1.2). The deviations should always be zero. In case of an overflow, the flag will be set differently and a correspondent deviation in b will be observed. Δp_{T}^{-1} should be bit-equivalent for all tracks.

5. Performance and applications

All performance results presented in this chapter are obtained via rerunning the AliRoot GTU simulation described in Section 3.4.2 on recorded data. As shown in Section 4.3, the simulation delivers bit equivalent results compared to the implemented hardware design. Hence, the presented performance reflects the expected performance in future data taking.

In the first part, the efficiency of the rejection of late conversion is presented. Prospects for the single electron triggers and the jet trigger follow in respective sections.

5.1. Rejection of late conversions

Since late conversions predominantly originate from the material in between TPC and TRD, they are most likely not matched to TPC tracks in the global off-line reconstruction. The rejection performance can thus be determined by comparing Δp_T^{-1} of on-line tracks which are matched to TPC tracks to Δp_T^{-1} of on-line tracks which are not matched. As mentioned in Section 3.3 the non-matched tracks partly originate from primary tracks which are not matched to TRD tracks due to matching inefficiencies. This is taken into account as described below.

The performance evaluation in this section is based on a minimum bias data sample from the period LHC15f (p-p, $\sqrt{s} = 13$ TeV). The Δp_T^{-1} distributions for all on-line TRD tracks with $p_T^{\text{on-line}} > 2$ GeV are shown in Figure 5.1a-c, respectively for tracks consisting of 4, 5, and 6 tracklets. The matched tracks are evenly distributed around zero, whereas the unmatched tracks show a double peak structure with local maxima at $\Delta p_T^{-1} \approx \pm 1$ c/GeV. The p_T resolutions for both the sagitta method and the straight line fit improve with a higher number of tracklets for the track. Hence, the Δp_T^{-1} distributions are narrowest for tracks consisting of 6 tracklets.

In addition, a peak around zero for unmatched tracks consisting of 5 and 6 tracklets is clearly visible. The peak arises from the aforementioned matching inefficiencies from TRD to TPC tracks, which have been observed before and amount to about 10 - 15% of the total number of matched tracks [31]. For these tracks the Δp_T^{-1} distributions are expected to be evenly distributed around zero as they also are for the matched tracks. To determine the rejection efficiency only for the late conversions, the unmatched tracks originating from matching inefficiencies are ignored: A Gaussian function is fitted to each of the three peaks in the Δp_T^{-1} spectra for tracks consisting of 5 and 6 tracklets, respectively. This is shown exemplary for the 6 tracklet case in Figure 5.1d. The peak arising from matching inefficiencies is subtracted from the spectrum. For tracks consisting of 4 tracklets, the matching inefficiencies are not separable from the rest of the unmatched

5. Performance and applications

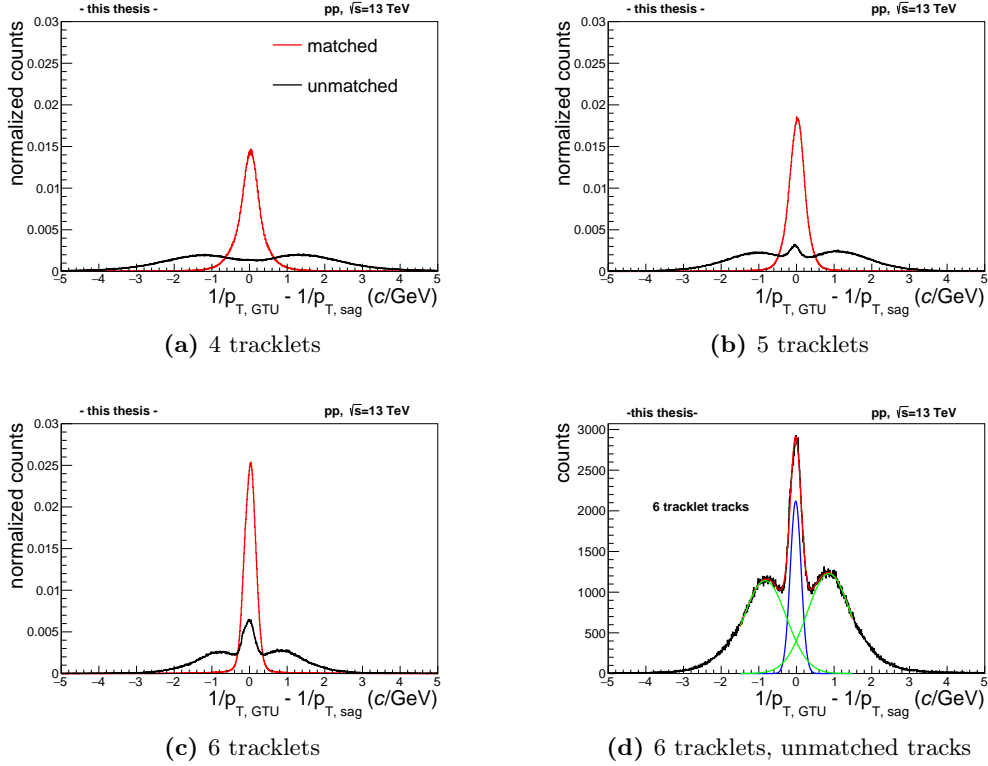


Figure 5.1.: These plots show the Δp_T^{-1} distribution for TRD tracks with $p_T^{\text{on-line}} > 2 \text{ GeV}/c$ for different numbers of tracklets in the track normalized to the respective track counts (a)-(c). Tracks with a matching track in the TPC are drawn in red, unmatched tracks in black. As can be seen from the plots, a cut on $|\Delta p_T^{-1}|$ enables the rejection of most of the unmatched tracks, while at the same time most of the matched tracks are kept. The peak for unmatched tracks around zero arises from matching inefficiencies from TRD to TPC tracks. These tracks are ignored for the performance evaluation of the late conversion rejection as shown in (d). A triple Gaussian (red) is fitted to the unnormalized spectra and the tracks not matched to TPC tracks due to matching inefficiencies (blue) are subtracted.

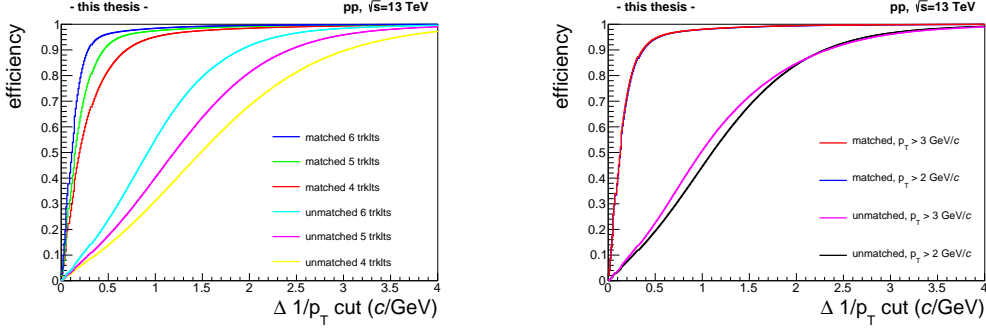


Figure 5.2.: The fraction of tracks passing a specific Δp_T^{-1} cut are shown on the left. All on-line tracks with $p_T^{\text{on-line}} > 2$ GeV/c are selected. The right plot shows the combined efficiency for tracks consisting of 5 or 6 tracklets and with transverse momenta in excess of 2 GeV/c, and 3 GeV/c, respectively. These are the decisive results for the single electron triggers. E.g. a cut at $\Delta p_T^{-1} < 0.2$ c/GeV for on-line tracks with $p_T > 3$ GeV/c and 5 or 6 tracklets results in an efficiency of 73% for the matched tracks and an efficiency below 9% for the unmatched tracks that do not originate from matching inefficiencies.

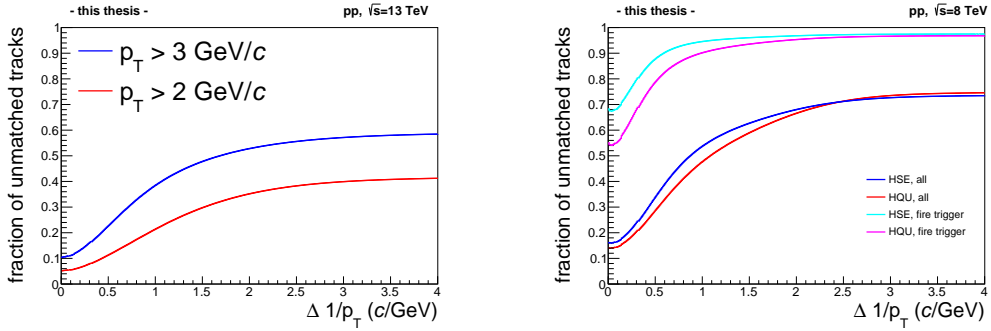


Figure 5.3.: The overall fraction of unmatched tracks in the data sample can be reduced significantly by the use of the late conversion rejection. This is shown on the left for the minimum bias data sample and for different track- p_T . The plot on the right shows the overall fraction of unmatched tracks for HQU and HSE triggered data from LHC12h. The red and blue curves represent all tracks with $p_T > 2$ GeV/c, the green and yellow curves represent only the tracks which comply with the respective trigger conditions.

5. Performance and applications

tracks in the sample. Thus, no tracks from the Δp_T^{-1} spectrum for unmatched tracks consisting of 4 tracklets are ignored.

It is now possible to compare the fraction of matched tracks passing the Δp_T^{-1} cut¹ to the fraction of unmatched tracks passing the same cut (see Figure 5.2).

The fraction of tracks surviving the cut increases with a higher number of tracklets in the track. This is expected from the distributions shown in Figure 5.1, since the curves narrow with a higher number of tracklets. Furthermore, the amount of matched tracks with a transverse momentum in excess of $p_T > 2 \text{ GeV}/c$ is almost identical to the amount of tracks with $p_T > 3 \text{ GeV}/c$ that pass the same cut. The same holds for the unmatched tracks in the regime of $\Delta p_T^{-1} < 0.2 \text{ c/GeV}$. For less stringent cuts ($0.2 \text{ c/GeV} < \Delta p_T^{-1} < 2 \text{ c/GeV}$) the fraction of unmatched tracks passing the cut is higher for tracks with a higher $p_T^{\text{on-line}}$. E.g. a threshold of $\Delta p_T^{-1} < 0.5 \text{ c/GeV}$ for tracks with $p_T > 3 \text{ GeV}/c$ results in an efficiency for matched tracks above 91%, whereas more than 82% of the unmatched tracks are rejected.

The importance of the late conversion rejection becomes evident, if the absolute quantity of unmatched tracks is compared to the quantity of matched tracks. In the analysed minimum bias sample the overall fraction of unmatched tracks of all tracks found by the TRD is $\sim 40\%$ for tracks with $p_T > 2 \text{ GeV}/c$ and $\sim 60\%$ for tracks with $p_T > 3 \text{ GeV}/c$ (see Figure 5.3a).

In LHC Run 1 the single electron triggers of the TRD (HQU and HSE) have been active in several data taking periods (for a detailed list see [26]). Results of the late conversions rejection for the HQU and HSE triggered events from the the p-p run at $\sqrt{s} = 8 \text{ TeV}$, namely from the data taking period LHC12h, are shown in Figure 5.3. The fraction of unmatched tracks in this sample is above 70%. Applying the late conversion rejection with a cut at $\Delta p_T^{-1} < 0.2 \text{ c/GeV}$ reduces the fraction of unmatched tracks for the HQU triggered data from 73% to 17% and from 73% to 20% for the HSE triggered data. The fractions of unmatched tracks which fulfill the trigger conditions $p_T \geq 2 \text{ GeV}$ ($\geq 3 \text{ GeV}$), $\text{PID} \geq 164$ (≥ 144), at least 5 tracklets and a tracklet in the first layer for the HQU (HSE) trigger is even above 97% for both triggers without a cut in Δp_T^{-1} . This interferes with a meaningful trigger operation.

In summary, the performance of the single electron triggers of the TRD will profit greatly from the rejection of late conversions. Introducing the new cut parameter Δp_T^{-1} results in the rejection of most of the late conversions. Thus, the rejection of the triggers are maintained while simultaneously the efficiency is increased, since the PID thresholds are lowered and the requirement of a tracklet in the first layer is dropped.

5.2. Prospects for electron triggers

The performance of rare triggers depends on two factors, namely the *efficiency* and the *purity*. An ideal trigger would accept every event of the specific physical interest (100% efficiency) and reject every other event (100% purity).

¹Note, that $\Delta p_T^{-1} := |p_{T,\text{GTU}}^{-1} - p_{T,\text{sag}}^{-1}|$ (see Section 3.3).

In the following, the performance of the single electron triggers of the TRD is analyzed. A minimum bias data sample is taken as a reference. Events containing electrons with a transverse momentum above the respective trigger threshold are considered the events of interest. The efficiencies of the triggers are thus obtained by determining the fraction of these events of interest which would be triggered by the TRD.

The purities of the triggered samples can be estimated by scaling the number of found electrons with a transverse momentum above the trigger threshold in the triggered sample by the number of triggered events. Since an event may contain more than one high- p_T electron, this is not the exact purity, but can serve as approximation.

The triggered event samples are obtained via simulating different trigger conditions. The p_T thresholds are kept at $p_T > 2$ GeV for the quarkonia trigger (HQU) and at $p_T > 3$ GeV for the single electron trigger (HSE). To arrive at a reasonable rejection, TRD tracks with less than 5 tracklets are ignored. The requirement of a tracklet in the first layer is dropped. The PID and Δp_T^{-1} parameters are varied in a broad range.

5.2.1. Event and track selection

The performance evaluation is based on the p-p data taking period LHC15f. The last supermodule of the TRD was installed in November 2014. Thus, the TRD covers the full central barrel acceptance for this data taking period. Minimum bias events are selected via requesting a coincident signal in the V0-A and V0-C detectors. To calculate reasonable rejection factors for the TRD triggers, it has to be ensured that the TRD is contained in the readout cluster. Hence, at least one of the following combinations of detectors had to be read out for the minimum bias trigger classes: **UFAST**, i.e. all central barrel detectors at least as fast as the TPC, **CENT**, i.e. all central barrel detectors or **ALL**, i.e. all detectors.

Electrons are identified via the TPC and TOF detectors with cuts on the N_σ values. For the TPC, this value is defined as follows:

$$N_\sigma^{\text{TPC}} = \frac{dE/dx_{\text{measured}} - dE/dx_{\text{expected}}}{\sigma_{\text{exp}}}. \quad (5.1)$$

The measured energy loss of the tracks is compared to the expected energy loss of the chosen particle species (depending on its momentum). This deviation is divided by the detector resolution σ_{exp} .

For TOF, the time of flight t^{tof} is explored:

$$N_\sigma^{\text{TOF}} = \frac{t_{\text{measured}}^{\text{tof}} - t_{\text{expected}}^{\text{tof}}}{\sigma_{\text{exp}}}. \quad (5.2)$$

The applied N_σ cuts are the following:

- $0 < N_{\sigma,e}^{\text{TPC}} < 3$
- $-3 < N_{\sigma,e}^{\text{TOF}} < 3$
- $N_{\sigma,\pi}^{\text{TPC}} < -4$

5. Performance and applications

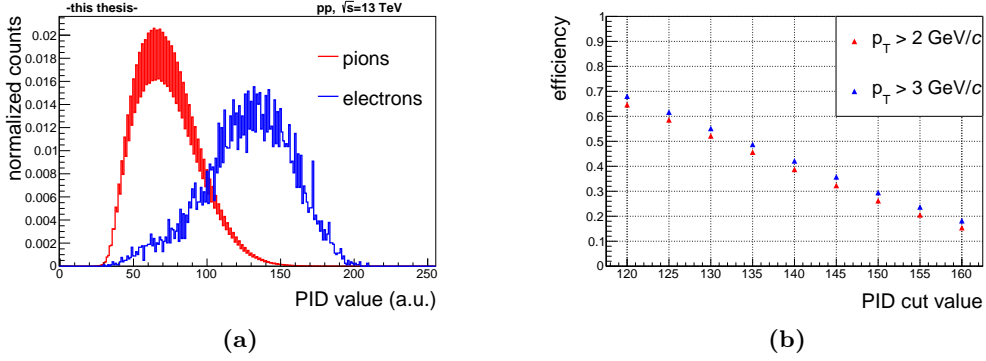


Figure 5.4.: The PID distribution for identified electrons and pions is shown on in (a). The observed binning effect originates from the use of the new look-up table. The resulting cut efficiency for electrons with $p_T > 2 \text{ GeV}/c$ (red) and $p_T > 3 \text{ GeV}/c$ (blue) is shown in (b). For electrons with $p_T > 3 \text{ GeV}/c$ the efficiency is slightly higher.

- $4 < N_{\sigma,\pi}^{\text{TPC}}$

The last two cuts are applied to achieve additional pion exclusion. Therefore, a very clean electron sample is obtained. In the regime of very high p_T the pion and electron bands are close, thus very high- p_T electrons are also rejected by this cut. However, this is not critical in the p_T range relevant for the TRD triggers. Additional track quality cuts are applied and primary particles are selected: A minimum number of found clusters in the TPC is required as well as a refit of the track in the ITS and the TPC and a threshold on the production vertex of $|z| < 2 \text{ cm}$ with respect to the primary vertex is set². These cuts result in a total number of ~ 9000 identified primary electrons with $p_T > 2 \text{ GeV}/c$ in the analyzed minimum bias data sample of $42 \cdot 10^6$ events.

5.2.2. PID and Δp_T^{-1} cut efficiencies

Before the overall performance is presented, the efficiencies for individual cuts on PID and Δp_T^{-1} are discussed. During data taking with the TRD in 2015, the deposited charge of the particles is translated via a linear look-up table and stored in the on-line PID values of the TRD tracks. The PID values thus do not represent the electron probability. Based on the LHC15f minimum bias data sample a non-linear look-up table was generated to translate the deposited charge directly into an electron probability in future data taking [30]. This new look-up table is used in this thesis for the evaluation of the trigger performance.

The PID distribution for electrons and pions is shown in Figure 5.4a. The total number of pions exceeds the total number of electrons by a factor larger than 300. Thus, a PID threshold below 120 results in a high pion contamination of the triggered sample. The

²The track cuts are obtained via `AliESDtrackCuts::GetStandardITSTPCTrackCuts2011(Bool_t selPrimaries = kTRUE, Int_t clusterCut = 1)`.

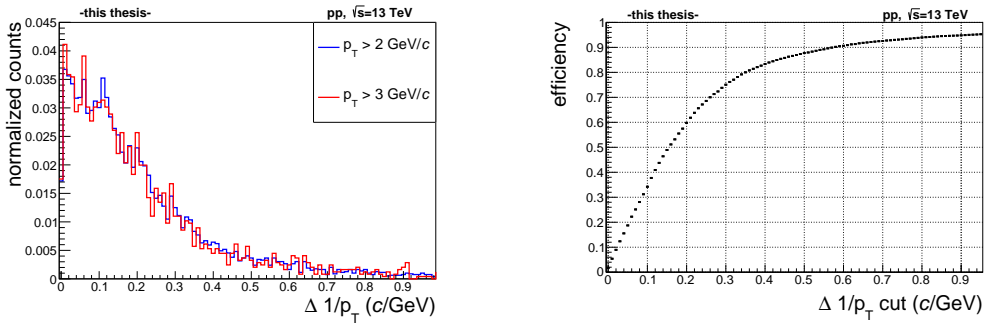


Figure 5.5.: The left plot shows the absolute value of Δp_T^{-1} for identified electrons. The resulting cut efficiencies for electrons with $p_T > 2 \text{ GeV}/c$ is shown on the right. The efficiency for electrons with $p_T > 3 \text{ GeV}/c$ is almost identical.

fraction of electrons from the sample defined in Section 5.2.1 which survives a specific cut on the PID value is shown in Figure 5.4b. The efficiency for a cut at 120 is $\sim 65\%$ and decreases almost linearly to about $\sim 15\%$ for a cut at 160.

The Δp_T^{-1} distribution for the primary electrons and the resulting efficiency for a cut on Δp_T^{-1} is shown in Figure 5.5. As expected from Figure 5.2, the efficiency for electrons with $p_T > 2 \text{ GeV}/c$ is almost identical to the efficiency for electrons with $p_T > 3 \text{ GeV}/c$. A threshold of $\Delta p_T^{-1} < 0.2 \text{ c/GeV}$ leads to an electron efficiency of $\sim 60\%$. For stricter cuts the efficiency decreases almost linearly to zero.

5.2.3. Results

As described above, the performance of rare triggers is determined by the efficiency and the purity. The latter does not necessarily need to be very high. As long as the available disk space and readout bandwidth suffice, events which are not of specific physical interest may be recorded as well. Rejection factors for the different triggers are introduced to take into account the limits of readout bandwidth and disk space. Naturally, they also depend on the expected rate of the rare events of interest. For both the HQU and the HSE triggers a rejection of about 10^3 is required and thus approximately adjusted for the performance estimates. In case a lower rejection is feasible, a higher efficiency would also be possible.

The event rejection factors for the single electron triggers of the TRD with regard to different trigger conditions are shown in Figure 5.6. To arrive at a rejection of 10^3 without a cut in Δp_T^{-1} is not feasible (At least not without the requirement of a tracklet in the first layer). The late conversion rejection allows for a much lower PID threshold compared to the trigger conditions in Run 1. Setting thresholds to $\Delta p_T^{-1} < 0.2 \text{ c/GeV}$ and $\text{PID} > 140$ results in a rejection of ~ 850 .

For these thresholds, the trigger performance is evaluated as follows: The p_T spectrum for all identified primary electrons in the minimum bias sample is plotted together with the p_T spectrum for the remaining primary electrons contained in the triggered event

5. Performance and applications

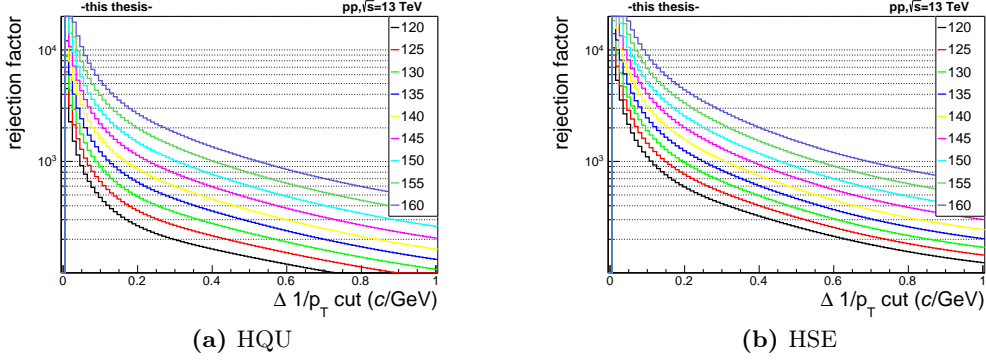


Figure 5.6.: Rejection factors for different trigger settings. A rejection of 10^3 means every 1000th event is triggered. The Δp_T^{-1} threshold is varied along the x -axis. Different PID thresholds are represented by different line colors (see legend). Only the p_T cut thresholds are fixed ($p_T > 2$ GeV for HQU and $p_T > 3$ GeV for HSE). For any combination of PID and Δp_T^{-1} thresholds the rejection can be retrieved directly from these plots.

sample (Figure 5.7a). Dividing both spectra results in the overall efficiency of the trigger (Figure 5.7b). Note, that in addition to the losses in efficiency induced from the track cuts, the efficiency times acceptance of the TRD results in a deterioration of the overall efficiency. For tracks consisting of 5 or 6 tracklets and with $p_T > 2$ GeV/ c the acceptance times efficiency is ~ 0.5 for electrons and ~ 0.6 for positrons [30].

Instead of the purity of the trigger, the enrichment of high- p_T primary electrons compared to the minimum bias sample is determined. The p_T spectra of the triggered event sample and of the minimum bias sample are normalized to the respective event counts (Figure 5.7c). Thus, the average number of electrons in the triggered event sample with a given p_T can be estimated from this plot. Note, that the average number of primary high- p_T electrons in the sample will be higher, since the track quality cuts and N_σ cuts cause additional losses in efficiency. However, these losses in efficiency cancel out when dividing the triggered spectrum by the minimum bias spectrum (Figure 5.7d). The shown enhancement and efficiency for the single electron triggers comprise the full performance of the TRD, i.e. acceptance times efficiency for tracks consisting of 5 and 6 tracklets and the efficiencies for the cuts in Δp_T^{-1} and PID.

To illustrate the power of the late conversion rejection, additional curves show the performance for a trigger with a lower Δp_T^{-1} cut, but a higher PID threshold, to arrive at a comparable rejection of ~ 800 . Furthermore, the performance of a trigger without late conversion rejection is shown. Both efficiency and enhancement deteriorate for the other trigger conditions, most significantly for the trigger without late conversion rejection.

The same is done for the HSE trigger (see Figure 5.8). A rejection of ~ 1000 is obtained by employing a threshold of $\Delta p_T^{-1} < 0.2$ c/GeV and a PID threshold of 130.

For both the HQU trigger and the HSE trigger the different trigger conditions with the resulting performances are summarized in Table 5.1. The values for efficiency and enhancement represent the median values of the correspondent curves. For the

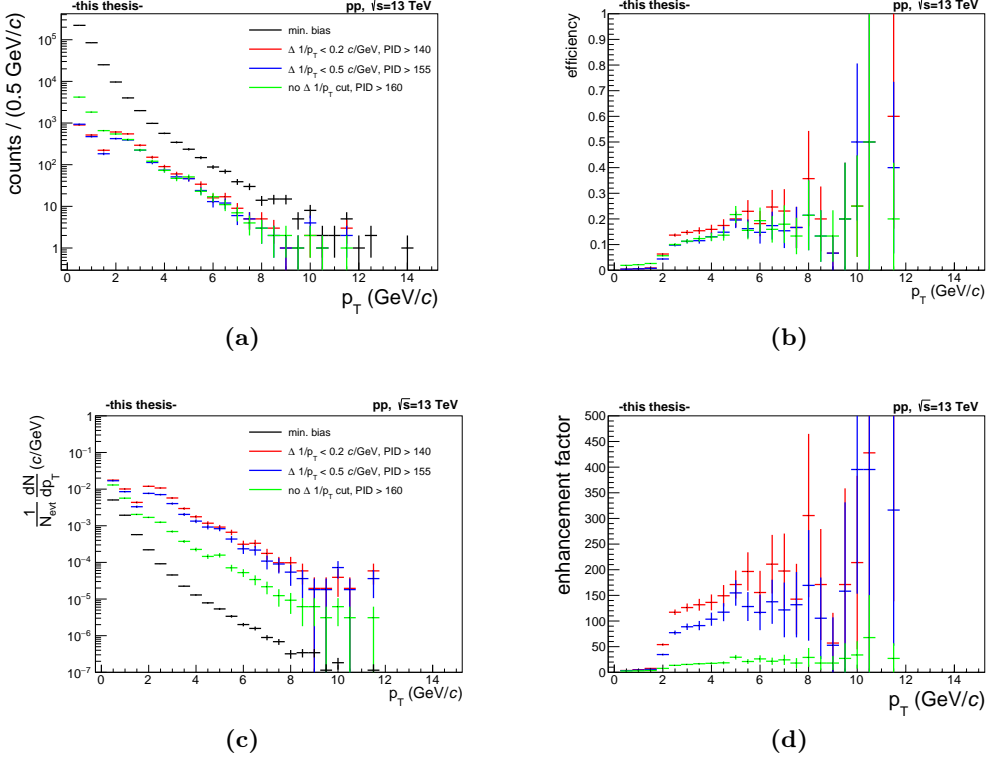


Figure 5.7.: HQU trigger performance ($p_{T,\text{thr}} = 2$ GeV/c). The p_T spectra for the min. bias sample (black) and triggered event samples are shown in **a)** for different trigger conditions (see legend). The efficiencies in **b)** are obtained by dividing the triggered spectra by the min. bias spectrum. In **c)** the p_T spectra are normalized to the respective event count to illustrate the electron enhancement compared to the min. bias sample plotted in **d)**. The optimal trigger conditions in terms of the overall efficiency (red) for a rejection of 855 are $\Delta p_T^{-1} < 0.2$ c/GeV and PID > 140. Two other trigger conditions are shown as a reference. The first one with a less stringent cut on Δp_T^{-1} (blue) results in a similar rejection. But as it can be seen from the plots, both the efficiency and the enhancement decrease compared to the red curve. The second one without a cut in Δp_T^{-1} (green) also results in a lower efficiency, although the rejection is only 135 and thus the enhancement diminishes. Therefore, reasonable rejection and efficiency simultaneously are not feasible for the HQU trigger without the late conversion rejection.

5. Performance and applications

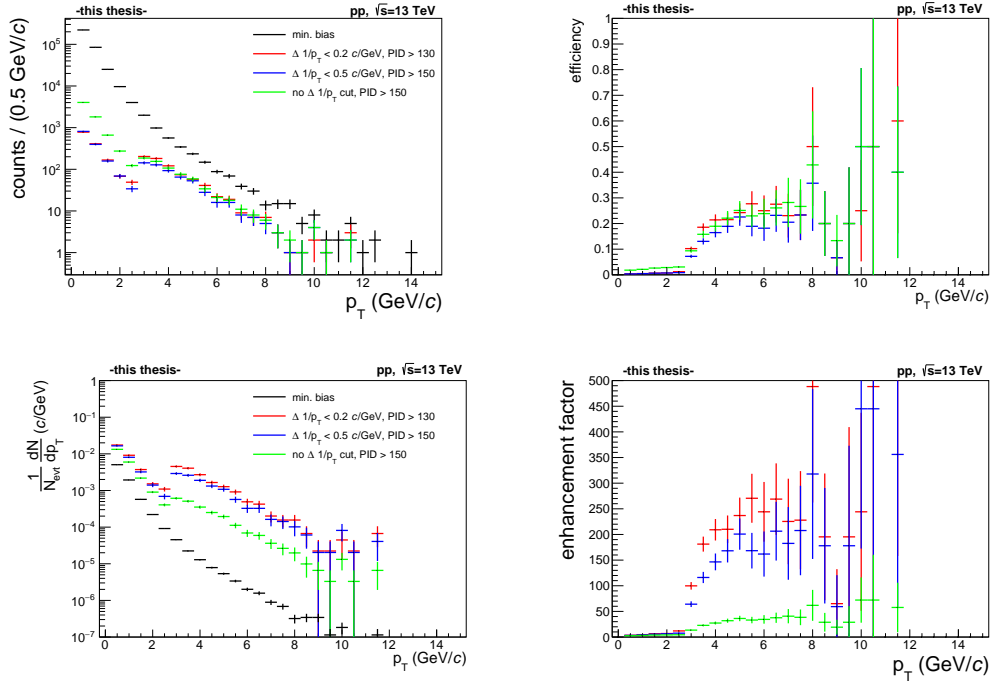


Figure 5.8.: HSE trigger performance ($p_{T,\text{thr}} = 3$ GeV/c). The plots are organized as in Figure 5.7. Again, the results for the optimal trigger conditions (red) are compared to a trigger with lower cut in Δp_T^{-1} but higher threshold for the PID value to arrive at a similar rejection (blue) and to a trigger without late conversion rejection (green). The rejection for the red and blue curves is about 900. As can be seen in (b), the efficiency of the green curve is comparable to the other triggers, whereas the enhancement clearly decreases as shown in (d), since the rejection recedes below 150.

trigger	thresholds	efficiency	enhancement	rejection
HQU	PID > 140 $\Delta p_T^{-1} < 0.2 \text{ c/GeV}$	0.15	127	855
	PID > 155 $\Delta p_T^{-1} < 0.5 \text{ c/GeV}$	0.11	87	790
	PID > 160 no cut in Δp_T^{-1}	0.15	16	135
HSE	PID > 130 $\Delta p_T^{-1} < 0.2 \text{ c/GeV}$	0.21	202	977
	PID > 150 $\Delta p_T^{-1} < 0.5 \text{ c/GeV}$	0.16	141	890
	PID > 150 no cut in Δp_T^{-1}	0.19	27	144

Table 5.1.: Overview of the different trigger conditions and the resulting performances. Efficiency and enhancement for the HQU triggers represent the median values for Figure 5.7b and Figure 5.7d, respectively, in the range $2.5 \text{ GeV}/c \leq p_T \leq 10 \text{ GeV}/c$. For the HSE trigger the median values in the range $3.5 \text{ GeV}/c \leq p_T \leq 10 \text{ GeV}/c$ are calculated from Figure 5.8b and Figure 5.8d.

HQU trigger the selected range is $2.5 \text{ GeV}/c \leq p_T \leq 10 \text{ GeV}/c$. For the HSE trigger $3.5 \text{ GeV}/c \leq p_T \leq 10 \text{ GeV}/c$ is chosen to incorporate the onset at higher p_T due to the higher p_T threshold of the trigger.

The resulting efficiency for the HQU trigger with a PID threshold of 140 and a Δp_T^{-1} threshold at 0.2 c/GeV is 15%. If a lower rejection is feasible, the thresholds could be relaxed to arrive at a higher efficiency. E.g. the same threshold of $\Delta p_T^{-1} < 0.2 \text{ c/GeV}$ and a PID threshold of 130 result in a efficiency of 23% and a rejection of ~ 500 . Note, that a lower threshold for the PID value leads to a higher gain in efficiency than a less stringent cut on Δp_T^{-1} (compare Figure 5.4 and Figure 5.5). The efficiency for the HSE trigger with a PID threshold of 130 and a Δp_T^{-1} cut at 0.2 c/GeV is 21%. Relaxing the PID threshold to 120 results in an efficiency of 26%, whereas the rejection is lowered to ~ 600 .

5.3. Jet trigger

The TRD provides a jet trigger (HJT) with the condition that 3 tracks with a transverse momentum in excess of $3 \text{ GeV}/c$ are found in a single stack. The high p_T threshold for the individual tracks results in a bias for the fragmentation functions of the leading jets with transverse momenta below $60 \text{ GeV}/c$ [26]. The fragmentation functions describe the p_T spectra for the tracks included in the jets for the respective jet- p_T . It is inspected, whether a different condition for HJT, i.e. a lower p_T threshold for the 3 tracks, only

5. Performance and applications

2 tracks per stack, or both, is feasible by applying the late conversion rejection and thus adding Δp_T^{-1} as cut parameter. A lower p_T threshold for the individual tracks or a lower number of tracks as condition for the trigger would reduce the bias on the jet fragmentation. However, without a cut in Δp_T^{-1} , the event rejection factor of the trigger was found to be too low for the trigger operation [40].

The performance evaluation is based on a minimum bias p–Pb data sample at $\sqrt{s_{\text{NN}}} = 5.023$ TeV from 2013 (LHC13c). This sample included $\sim 90 \cdot 10^6$ events with the TRD in the readout cluster.

The rejection factor for the HJT condition is found to be ~ 2000 . If the condition is relaxed to two tracks with $p_T > 3$ GeV/ c , the rejection decreases to below 200. Figure 5.9 shows the different rejection factors for varying track count, Δp_T^{-1} thresholds and a p_T threshold at 2 and 3 GeV/ c , respectively. As expected, the rejection factors for the trigger can be increased with stricter Δp_T^{-1} cut thresholds. Note, that the incomplete installation of the TRD for this period results in an additional factor of $^{13}/_{18}$ by which the rejection must be scaled to obtain the expectation for future data taking.

The effect of the additional cut in Δp_T^{-1} on the efficiency is shown in Figure 5.10. The presented p_T spectrum for charged jets in the minimum bias sample is obtained by the use of the anti-kt cluster finder algorithm for jets with a radius of $R = 0.4$ and $|\eta^{\text{jet}}| \leq 0.5$.

The performance evaluation for the jet trigger is currently under study. In the presented plots it is clearly visible, that a cut at $\Delta p_T^{-1} < 0.3$ c/GeV deteriorates the efficiency of the trigger. But the rejection is also increased. E.g. comparing the efficiency for the original HJT condition (Figure 5.10d, cyan curve) to the efficiency for a condition of two tracks above 3 GeV/ c plus a Δp_T^{-1} cut at 0.3 c/GeV (Figure 5.10b, green curve) increases the efficiency for jets in the p_T bin from 40 to 50 GeV/ c by $\sim 10\%$. The rejection on the other hand decreases by a factor of 0.23. The overall losses in efficiency can partially be explained by the impaired performance of the late conversion rejection for tracks consisting of only 4 tracklets. A strict cut in Δp_T^{-1} results in the loss of also a lot of the tracks which are matched to TPC tracks (see Figure 5.1).

Solely a loss in efficiency could be compensated for by recording a larger event sample with the trigger. It remains to be answered, whether the Δp_T^{-1} cut induces an additional bias for analyses, e.g., by evaluating the fragmentation functions for the leading jets.

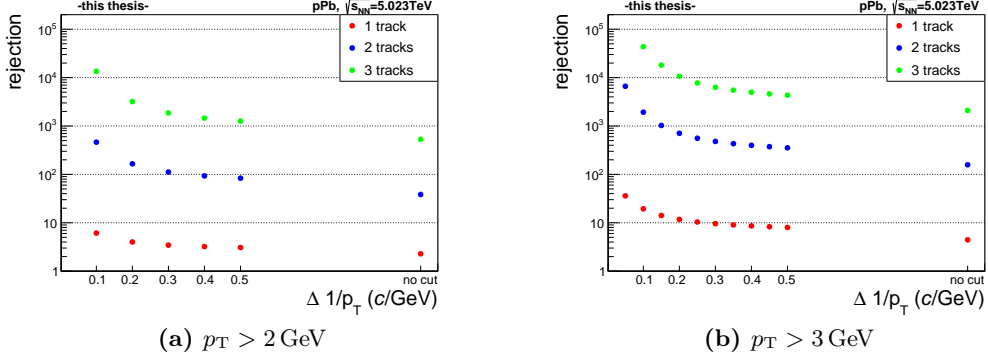


Figure 5.9.: Rejection factors regarding different numbers of tracks per stack and different cuts in Δp_T^{-1} . In (a) for a p_T threshold of 2 GeV/ c and in (b) for a p_T threshold of 3 GeV/ c .

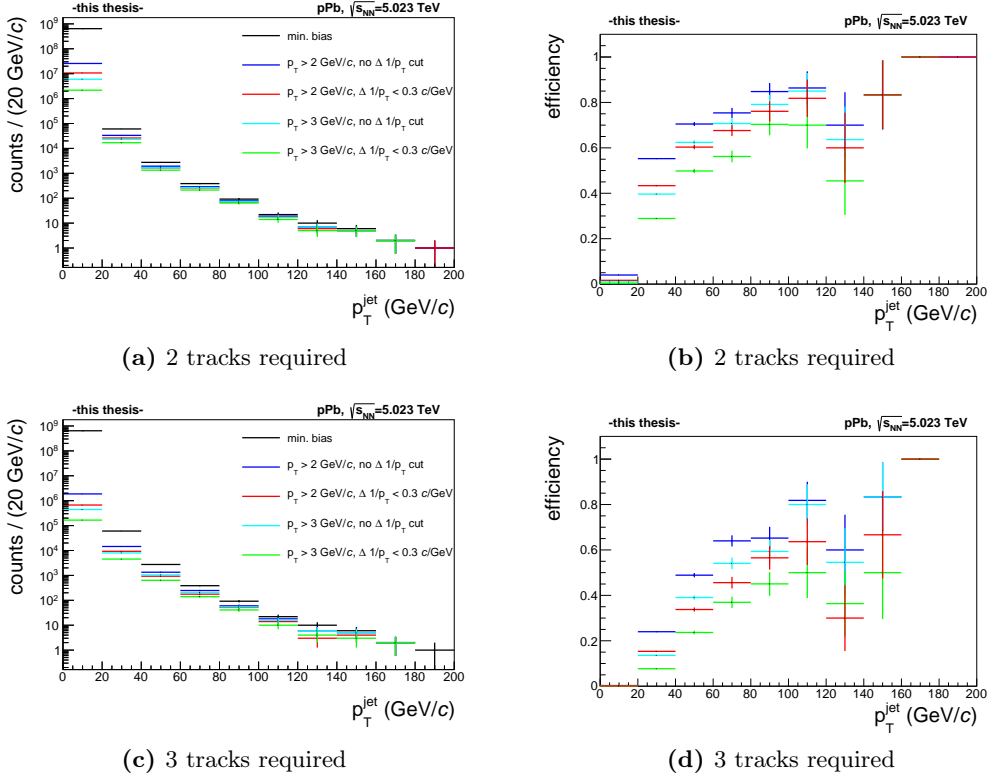


Figure 5.10.: The plots on the left show charged jet p_T spectra (anti-kt, $R = 0.4$, $|\eta^{\text{jet}}| \leq 0.5$) for the min. bias sample (black) and different triggered samples. The upper plot (a) requires two tracks with the conditions indicated in the legend, the lower plot (c) requires three. The right plots show the efficiencies obtained by dividing the respective triggered sample by the min. bias sample. The red and green curves represent trigger conditions with a Δp_T^{-1} cut at 0.3 c/GeV. For those curves, a loss in efficiency is clearly visible. On the other hand the rejection increases by a factor of ~ 3 compared to the respective curves without a Δp_T^{-1} cut.

6. Summary and Outlook

As well as particle tracking and electron identification, the TRD provides various trigger contributions at level-1. Photon conversions into electrons and positrons at large radii, mostly in the supporting structure in front of the TRD, caused the dominant background of the single electron triggers. These so-called *late conversions* are an order of magnitude likelier to fire the single electron triggers of the TRD than primary tracks.

It was proposed to exploit the local curvature of the tracks to identify these late conversions on-line, since it is much larger for these compared to primary electrons [30, 32]. This can be done via calculating the inverse transverse momentum from the sagitta of the tracks and comparing it to the inverse transverse momentum determined in the Global Tracking Unit (GTU) from the offset of a straight line fit of the track to the nominal vertex, introducing a new track parameter Δp_T^{-1} . A simplified algorithm well adapted for the fast on-line track reconstruction in hardware was found and implemented in the software simulation of the GTU. The necessary arithmetic operations were limited to 8 multiplications, 6 additions, 3 accesses to look-up tables and 1 comparison. A detailed block diagram was developed that served as template for the implementation in hardware, which in turn was performed by Felix Rettig [31]. Most of the calculations are executed in parallel, thus the algorithm was implemented employing only 5 internal pipeline stages. These pipeline stages are in turn parallel to already existing ones, therefore the overall latency of the track reconstruction is unchanged. Since the clock frequency of the reconstruction unit in the FPGA is 50 MHz, the computation latency of the algorithm is 100 ns.

The commissioning process firstly comprised an emulation of the hardware tracking with tracks from tracklet files as input. These were prepared specifically for this purpose. Tracks were selected from recorded data so as to cover all possible cases for the tracklet composition and different track parameters, e.g. p_T . The composing tracklets of these tracks were written to the files. Secondly, the FPGA designs were loaded into the GTU test setup in Heidelberg to ensure that the raw data readout is not affected by the extended track reconstruction algorithm. After successful testing, the late conversion rejection was activated during data taking of the experiment in Pb–Pb collisions. The hardware implementation was validated and the results agree with those of the software simulation on the bit-level.

The software simulation was then used to evaluate the performance of the late conversion rejection (as implemented in hardware) for a minimum bias p–p data sample at $\sqrt{s} = 13$ TeV (LHC15f.pass2). For tracks with $p_T > 2$ GeV/ c (3 GeV/ c) and 5 or more tracklets, 92% (91%) of the late conversions are rejected while the efficiency for tracks which are matched to TPC tracks is 72% (73%) for a cut at $\Delta p_T^{-1} < 0.2$ c/GeV. This allows us to lower the PID thresholds of the single electron triggers and addition-

6. Summary and Outlook

ally drop the requirement of a tracklet in the first layer. As a result, the rejections of the triggers are maintained, and the efficiencies simultaneously increase. Trigger conditions for both single electron triggers, i.e. the HQU and the HSE trigger, are proposed. The requirement of a track with at least 5 tracklets, $p_T > 2 \text{ GeV}/c$, $\text{PID} > 140$ and $\Delta p_T^{-1} < 0.2 \text{ c}/\text{GeV}$ results in an overall efficiency of 15% for primary electrons in the range $2.5 \text{ GeV}/c \leq p_T \leq 10 \text{ GeV}/c$ and a rejection factor of 855 for the HQU trigger. The overall efficiency next to the efficiency for the late conversion rejection also includes the PID cut efficiency and the acceptance times efficiency of the TRD. Omitting the cut in Δp_T^{-1} and increasing the PID threshold to 160 would lead to an equal efficiency at a rejection of only 135.

For the HSE trigger the following conditions for a track are proposed: $p_T > 3 \text{ GeV}/c$, $\text{PID} > 130$, $\Delta p_T^{-1} < 0.2 \text{ c}/\text{GeV}$ and also at least 5 tracklets. These conditions result in an efficiency of 21% in the p_T range from 3.5 to $10 \text{ GeV}/c$ and a rejection of 977. Omitting the Δp_T^{-1} cut and increasing the PID threshold to 150 reduces the efficiency to 19% although at the same time the rejection is reduced to 144.

The application of the late conversion rejection for the jet trigger was also studied. The goal was to relax either the p_T threshold, or the number of required tracks per stack, or both, to achieve an unbiased sample for jet p_T from $60 \text{ GeV}/c$ onwards. A cut in Δp_T^{-1} allowed more relaxed thresholds in p_T and the number of tracks as it increased the rejection for the trigger. But at the same time it reduced the efficiency for jets in the desired p_T range.

The results of this thesis were presented to the trigger coordination of the ALICE collaboration, as the trigger menu for data taking over the next years is currently under discussion and rare triggering with the TRD is foreseen during LHC Run 2. An exchange with the physics working groups is in progress to determine required trigger conditions. Further studies are needed for a full performance evaluation of the modified jet trigger, e.g. regarding the fragmentation of the triggered jets. The single electron triggers depend on the rejection of late conversions for a meaningful trigger operation.

Acknowledgements I would like to thank Prof. Dr. Johanna Stachel for giving me the opportunity to work on this particularly nice and diversified topic.

My special gratitude goes to Dr. Jochen Klein, who supported me continuously and from whom I have learned a lot throughout this time.

Furthermore, I want to heartily thank Uwe Westerhoff, Felix Rettig, Guido Willems and Prof. Peter Glässel for the close collaboration. I am indebted to Dr. Yvonne Pachmayer for her help with the operation of the analysis trains at GSI, especially in times when the results were very much-needed.

For proofreading of my thesis I would like to thank Dr. Jochen Klein, Dr. Yvonne Pachmayer, Michael Winn, Dr. Hans Beck, Jeremy Wilkinson, Prof. Peter Glässel, Dennis Weiser and Svenja Lohmann.

I also want to express my gratitude for many people from the group and from the ALICE collaboration.

Last but not least, I thank my parents for their support during my studies.

A. GTU simulation

A.1. Output of the late conversion rejection

The late conversion rejection is enabled by default for the AliRoot GTU simulation. If the results of the the calculation need to be written to the parameters b and c of the track word, e.g. in case different thresholds shall be tested for Δp_T^{-1} , the GTU simulation needs to be configured accordingly:

```
AliTRDgtuParam::WriteSagittaOutputToTrackWordBC(kTRUE)
```

To calculate Δp_T^{-1} from the track word in the analysis task, one can implement a function like this:

```
Float_t AliAnalysisTaskTRDgtuSim::GetInvPtDevFromTrackWordBC(Int_t b, Int_t c)
{
    Int_t tmp = (((b & 0xfff) << 12) ^ 0x800000) - 0x800000;
    tmp += (c & 0xfff);
    Float_t invPtDev = tmp * 0.000001;
    return invPtDev;
}
```

This returns Δp_T^{-1} in the unit c/GeV .

A.2. Performance for different optimization methods

The optimization methods for the sagitta calculation presented in Section 3.4.3 are analyzed in a minimum bias data sample of the p–Pb data taking period (LHC13b).

The GTU simulation can be configured via the class `AliTRDgtuParam` to enable the different optimizations:

```
AliTRDgtuParam::SetCorrectionMode(Int_t iMode);
```

The default value 0 corresponds to no optimization. This corresponds to the current implementation in hardware. The other values are listed in Table A.1.

The results of the different optimizations are shown in Figure A.1. For tracks consisting of 6 tracklets the electron efficiency increases while the rejection of late conversions remains constant. For tracks consisting of 5 tracklets on the other hand, the efficiencies for both electrons and late conversions increases simultaneously. Therefore, no optimizations are implemented in the hardware. The performance of the optimizations increases, if the length of the track in the TRD is not simply approximated with the distance covered in x [30]. But as mentioned in Section 3.4.3, this would also make the sagitta algorithm more complex.

iMode	optimizations
0	no corrections (default)
1	alignment correction and artificial tracklet removal
2	alignment correction and pad tilting correction
3	all of the above corrections combined

Table A.1.: Overview of the available optimization methods in the GTU simulation. The alignment correction is enabled for all corrections, since it will be implemented in the MCMs instead of the GTU and its effect is small.

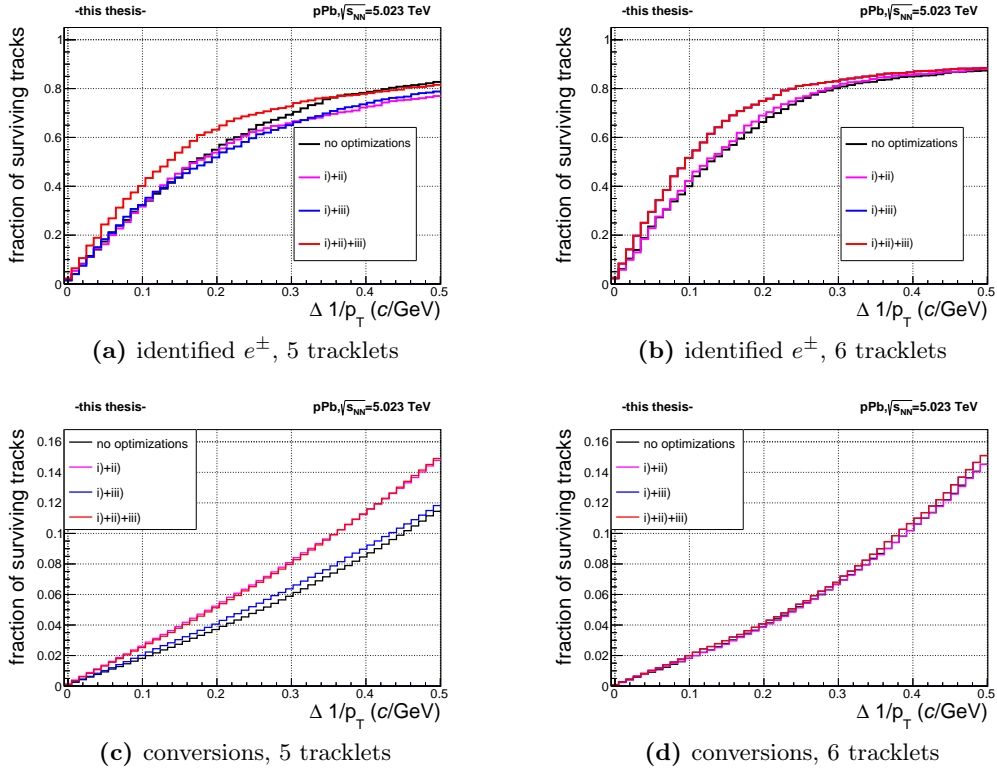


Figure A.1.: Effects of the different optimization methods for the $p_{T,\text{sag}}^{-1}$ calculation in the GTU simulation. While for tracks consisting of 6 tracklets the efficiency for the electrons increases and the rejection of late conversions remains constant (compare (b) and (d)), this is not the case for tracks consisting of only 5 tracklets. For those, the efficiencies for both electrons and late conversion increase (compare (a) and (c)). Shown are all tracks with $p_T^{\text{on-line}} > 2 \text{ GeV}/c$ and $\text{PID} > 130$. The correction modes are as follows: **i**) is the alignment correction, **ii**) is the artificial tracklet removal and **iii**) is the pad tilting correction.

```

# T1 = { -2, 2, 2, -2, 0, 0}, T2 = -14930, T3 = 421
# M1 = 3000, M2 = -4688, M3 = -4384, M4 = 3822, M5 = 0, M6 = 0
# M7 = 33592500, M8 = 61045
# A1 = -1688, A2 = -562, A3 = 0
# A4 = -2250, A5 = -2250, A6 = -33531455
# event: 1, TRD stack: S02-0
# notes: a: +580 ipt: +2108 pt: +16.468750
# data: 1 GTU tracks, L0 1/2/4/8/0/0 L5 tracklets
# GTU track: tw=0x0000000059c138 etw=0x00000000141149
# lm=0xf Abs(pt)=16.468750GeV/c a=+145(+580) PID=56
00001 02 0 0 0 0x10001000 0x10001000
00001 02 0 0 1 0x21285a24 0x10001000 0x10001000
00001 02 0 1 0 0x10001000 0x10001000
00001 02 0 1 1 0x1f15f6d8 0x10001000 0x10001000
00001 02 0 2 0 0x10001000 0x10001000
00001 02 0 2 1 0x49173770 0x10001000 0x10001000
00001 02 0 3 0 0x10001000 0x10001000
00001 02 0 3 1 0x58159889 0x10001000 0x10001000
00001 02 0 4 0 0x10001000 0x10001000
00001 02 0 4 1 0x10001000 0x10001000
00001 02 0 5 0 0x10001000 0x10001000
00001 02 0 5 1 0x10001000 0x10001000

```

Figure A.2.: Content of an ASCII file which can be used as input for the GTU simulation. The upper lines in blue are comments and ignored by the simulation. The columns represent from left to right: event number, sector, stack, layer, link and the tracklet words in hexadecimal notation. The sequence 0x10001000 0x10001000 is used as tracklet end marker.

A.3. Load custom tracklet files

For the commissioning process of the late conversion rejection, custom tracklet files in the ASCII file format are created which serve as input for both the hardware and the software simulation. The tracklet files need to be of the form as shown in Figure A.2. The results of the intermediate steps of the sagitta calculation are added as a comment to the tracklet file. T denotes the look-up tables, M the multiplications and A the additions. E.g. the value A6 corresponds to Δp_T^{-1} in the unit $10^{-6} c/\text{GeV}$.

Bibliography

- [1] M. Thomson. *Modern Particle Physics*. Cambridge University Press, 2013.
- [2] M. L. Perl, E. R. Lee, and D. Loomba. *Searches for fractionally charged particles*. In: Annual Review of Nuclear and Particle Science 59.1 (2009), p. 47.
- [3] K. A. Olive, P. D. Group, et al. *Review of particle physics*. In: Chinese Physics C 38.9 (2014), p. 090001.
- [4] N. Cabibbo and G. Parisi. *Exponential hadronic spectrum and quark liberation*. In: Physics Letters B 59.1 (1975), pp. 67–69.
- [5] J. C. Collins and M. J. Perry. *Superdense matter: neutrons or asymptotically free quarks?* In: Physical Review Letters 34.21 (1975), p. 1353.
- [6] W. Reisdorf and H. Ritter. *Collective flow in heavy-ion collisions*. In: Annual Review of Nuclear and Particle Science 47.1 (1997), pp. 663–709.
- [7] K. Aamodt et al. *Elliptic flow of charged particles in Pb-Pb collisions at 2.76 TeV*. In: Phys. Rev. Lett. 105 (2010), pp. 252–302.
- [8] G. B. Perkins Donald H. *Introduction to high energy physics*. Vol. 2. Addison-Wesley Reading, Massachusetts, 1982.
- [9] T. S. Pettersson, P. Lefevre, L. S. Group, et al. *The large hadron collider: conceptual design*. In: CERN, Geneva, Tech. Rep. CERN-AC-95-05 LHC (1995).
- [10] *The Large Hadron Collider*. <http://home.cern.ch/topics/large-hadron-collider>. Online; accessed Dec. 19, 2015.
- [11] G. Aad et al. *Observation of a new particle in the search for the Standard Model Higgs boson with the ATLAS detector at the LHC*. In: Physics Letters B 716.1 (2012), pp. 1–29.
- [12] S. Chatrchyan et al. *Observation of a new boson at a mass of 125 GeV with the CMS experiment at the LHC*. In: Physics Letters B 716.1 (2012), pp. 30–61.
- [13] P. Mouche. *Overall view of the LHC*. Dec. 6, 2014. URL: <https://cds.cern.ch/record/1708847?ln=de>.
- [14] N. Antoniou et al. *Letter of intent for a large ion collider experiment*. In: CERN/LHCC (1993), pp. 93–16.
- [15] ALICE Collaboration. *Technical proposal for A Large Ion Collider Experiment at the CERN LHC*. LHC Tech. Proposal CERN-LHCC-95-71. Geneva: CERN, 1995.
- [16] ALICE Collaboration. *Technical Design Report of the Inner Tracking System*. Tech. rep. CERN-LHCC-99-12. Geneva, 1999.

Bibliography

- [17] ALICE Collaboration. *Technical Design Report of the Time Projection Chamber*. Tech. rep. CERN-LHCC-2000-001. Geneva, 2000.
- [18] J. Alme et al. *The ALICE TPC, a large 3-dimensional tracking device with fast readout for ultra-high multiplicity events*. In: Nucl. Instrum. Meth. A622 (2010), pp. 316–367.
- [19] P. Cortese et al. *ALICE transition-radiation detector: Technical Design Report*. Technical Design Report ALICE. Geneva: CERN, 2001.
- [20] P. Cortese et al. *ALICE: Addendum to the technical design report of the time of flight system (TOF)*. In: CERN-LHCC-2002-016 (2002).
- [21] B. Chang et al. *Rapidity and transverse-momentum dependence of the inclusive J/ψ nuclear modification factor in p-Pb collisions at $\sqrt{s_{\text{NN}}} = 5.02$ TeV*. 2015. arXiv: 1503.07179 [nucl-ex].
- [22] B. B. Abelev et al. *Performance of the ALICE Experiment at the CERN LHC*. In: Int. J. Mod. Phys. A29 (2014), p. 1430044. DOI: 10.1142/S0217751X14300440. arXiv: 1402.4476 [nucl-ex].
- [23] G. Dellacasa and P. Braun-Munzinger. *ALICE: a transition radiation detector for electron identification within the ALICE central detector - an addendum to the Technical Proposal*. Tech. rep. CERN-LHCC-99-013. LHCC-P-3-Add-2. Geneva: CERN, May 1999.
- [24] V. L. Ginzburg and I. M. Frank. *Radiation of a uniformly moving electron due to its transition from one medium into another*. In: J. Phys.(USSR) 9 (1945), pp. 353–362.
- [25] A. Andronic et al. *The ALICE Transition Radiation Detector: construction, operation, and performance in LHC Run 1*. In preparation.
- [26] J. Klein. *Jet Physics with A Large Ion Collider Experiment at the Large Hadron Collider*. Doctoral thesis, Heidelberg University. 2014.
- [27] J. Klein. *Commissioning of and Preparations for Physics with the Transition Radiation Detector in A Large Ion Collider Experiment at CERN*. Diploma thesis, Heidelberg University. 2008.
- [28] J. de Cuveland. *Entwicklung der globalen Spurrekonstruktionseinheit für den ALICE-Übergangsstrahlungsdetektor am LHC (CERN)*. Diplomarbeit, Universität Heidelberg, Germany. 2003.
- [29] M. Walter. *Performance of Online Tracklet Reconstruction with the ALICE TRD*. Diploma thesis, Münster University. 2010.
- [30] U. Westerhoff. *No title*. Doctoral thesis, in preparation.
- [31] F. Rettig. *The Global On-line Tracking and Trigger System for the ALICE Transition Radiation Detector at the Large Hadron Collider*. Doctoral thesis, in preparation.
- [32] P. Glaessel. private communication.

- [33] K. Kleinknecht. *Detektoren für Teilchenstrahlung*. Springer-Verlag, 2005.
- [34] D. Hanke-Bourgeois Martin. *Grundlagen der Numerischen Mathematik und des Wissenschaftlichen Rechnens*. Vol. 3. Teubner-Verlag, Stuttgart, 2002.
- [35] Root. URL: <https://root.cern.ch/>.
- [36] ALICE Collaboration. URL: <http://aliweb.cern.ch/Offline/AliRoot/Manual.html>.
- [37] J. de Cuveland. *A Track Reconstructing Low-latency Trigger Processor for High-energy Physics*. Doctoral thesis, Heidelberg University. 2009.
- [38] S. Kirsch. *High-Speed Event-Buffered Read-Out for the ALICE TRD*. Doctoral thesis, in preparation.
- [39] J. Klein. *Triggering with the ALICE TRD*. In: Nucl. Instrum. Meth. A706 (2013), pp. 23–28. DOI: 10.1016/j.nima.2012.05.011. arXiv: 1112.5110 [nucl-ex].
- [40] J. Klein. private communication.

Statement of Originality (Erklärung):

I certify that this thesis, and the research to which it refers, are the product of my own work. Any ideas or quotations from the work of other people, published or otherwise, are fully acknowledged in accordance with the standard referencing practices of the discipline.

Ich versichere, dass ich diese Arbeit selbständig verfasst und keine anderen als die angegebenen Quellen und Hilfsmittel benutzt habe.

Heidelberg, March 1, 2016

.....
(signature)